

Modeling intrinsic galaxy alignment in the MICE simulationKai Hoffmann^{1,2,*}, Lucas F. Secco,³ Jonathan Blazek,⁴ Martin Crocce,^{1,5} Pau Tallada-Crespí,^{6,7} Simon Samuroff,⁴ Judit Prat,^{3,8} Jorge Carretero,^{9,7} Pablo Fosalba,^{1,5} Enrique Gaztañaga,^{1,5} and Francisco J. Castander^{1,5}

(DES Collaboration)

¹*Institute of Space Sciences (ICE, CSIC), Campus UAB, Carrer de Can Magrans, s/n, 08193 Barcelona, Spain*²*Institute for Computational Science, University of Zurich, Winterthurerstr. 190, 8057 Zürich, Switzerland*³*Kavli Institute for Cosmological Physics, University of Chicago, Chicago, Illinois 60637, USA*⁴*Department of Physics, Northeastern University, Boston, Massachusetts 02115, USA*⁵*Institut d'Estudis Espacials de Catalunya (IEEC), 08034 Barcelona, Spain*⁶*Centro de Investigaciones Energéticas, Medioambientales y Tecnológicas (CIEMAT), Avenida Complutense 40, 28040 Madrid, Spain*⁷*Port d'Informació Científica (PIC), Campus UAB, C. Albareda s/n, 08193 Barcelona (Barcelona), Spain*⁸*Department of Astronomy and Astrophysics, University of Chicago, Chicago, Illinois 60637, USA*⁹*Institut de Física d'Altes Energies (IFAE), The Barcelona Institute of Science and Technology, Campus UAB, 08193 Barcelona, Spain*

(Received 29 June 2022; accepted 18 October 2022; published 21 December 2022)

The intrinsic alignment (IA) of galaxies is potentially a major limitation in deriving cosmological constraints from weak lensing surveys. In order to investigate this effect, we assign intrinsic shapes and orientations to galaxies in the light-cone output of the MICE simulation, spanning ~ 5000 deg² and reaching redshift $z = 1.4$. This assignment is based on a semianalytic IA model that uses photometric properties of galaxies as well as the spin and shape of their host halos. Advancing on previous work, we include more realistic distributions of galaxy shapes and a luminosity-dependent galaxy-halo alignment. The IA model parameters are calibrated against COSMOS and BOSS LOWZ observations. The null detection of IA in observations of blue galaxies is accounted for by setting random orientations for these objects. We compare the two-point alignment statistics measured in the simulation against predictions from the analytical IA models NLA and TATT over a wide range of scales, redshifts, and luminosities for red and blue galaxies separately. We find that both models fit the measurements well at scales above $8 h^{-1}$ Mpc, while TATT outperforms NLA at smaller scales. The IA parameters derived from our fits are in broad agreement with various observational constraints from red galaxies. Lastly, we build a realistic source sample, mimicking DES Year 3 observations and use it to predict the IA contamination to the observed shear statistics. We find this prediction to be within the measurement uncertainty, which might be a consequence of the random alignment of blue galaxies in the simulation.

DOI: [10.1103/PhysRevD.106.123510](https://doi.org/10.1103/PhysRevD.106.123510)**I. INTRODUCTION**

Weak gravitational lensing, able to directly probe dark-matter-dominated large-scale structures in the Universe, has become a core cosmological probe [1–3]. In the coming years, next-generation experiments, including Euclid, the Vera C. Rubin Observatory, and the Nancy Grace Roman Space Telescope, will rely on weak lensing to provide a substantial part of their overall constraining power. However, weak lensing analyses bring several challenges, including both measurement methodology and understanding complex astrophysical effects. One of the main astrophysical effects is the intrinsic alignment (hereafter also

referred as IA) of source galaxies [e.g., [4–7]], which contaminates the alignment signal induced by gravitational lensing. Understanding how IA affects the observed weak lensing statistics is becoming increasingly important as the statistical errors are decreasing strongly with the larger volumes probed by modern surveys. It has been shown that ignoring IA can bias the constraints on cosmological parameters from these lensing surveys significantly [8]. The IA contribution therefore needs to be included in the modeling of the observed data when deriving cosmological constraints from weak lensing observations.

Analytic IA models [e.g., [9–13]] are typically used to mitigate the impact of IA on lensing measurements. However, it is not yet known which IA models are sufficiently accurate to avoid biasing cosmological

*kai.d.hoffmann@gmail.com

parameter inference. Alternatively, employing overly complex modeling can remove cosmological constraining power and might introduce parameter degeneracy. It is thus important to test if current IA models satisfy the accuracy requirements for the upcoming observations. One possibility to do so is provided by direct measurements of IA in spectroscopic surveys, as these surveys enable a clear separation between foreground and background galaxies. Such a separation is not possible with the less accurate photometric redshift estimates that are used in weak lensing surveys. Direct measurements of IA have been made in several spectroscopic surveys, including SDSS, WiggleZ, BOSS, KiDS + GAMA, and PAU [14–22], and revealed inaccuracies of the analytic IA models, in particular at small scales. These direct observations further showed that the IA signal depends strongly on the luminosity and color range probed by a given galaxy sample, indicating that the shapes and orientations of galaxies are affected by the same evolutionary processes (e.g., merging and cold gas accretion) that determine the photometric properties of galaxies. This conclusion lines up with results from hydrodynamic simulations [e.g., [23]]. The alignment contributions to the lensing signal are therefore expected to depend strongly on the photometric properties as well as on the redshift of the source samples used in weak lensing analysis. An assessment of how strongly inaccuracies of analytical IA models may bias the cosmological constraints derived from lensing surveys can therefore not be derived from the current spectroscopic IA observations, which are focused mainly on red galaxies at relatively low redshifts ($z \lesssim 0.5$).

This lack of observational IA constraints may be filled by cosmological simulations, which can provide insights into IA behavior and allow for testing of modeling and analysis methods in a realistic setting. Cosmological hydrodynamic simulations of galaxy formation can predict the alignment of galaxies as a function of color and luminosity up to high redshifts [24–28]. However, their relatively low resolution as well as the assumptions involved in the implementations of galaxy formation processes may impose a bias on the IA constraints derived from these simulations, which has not been investigated so far. In addition, the volumes covered by these simulations are several orders of magnitudes below those probed by lensing surveys due to computational limitations, which inhibits investigations at the large scales probed in observations.

The need for simulating IA in large cosmological volumes promoted the development of models, which assign intrinsic shapes and orientations to galaxies that were placed in dark-matter-only simulations using approximate methods. These models (hereafter referred to as semianalytic IA models) are based on the assumption that each galaxy can be described either as a disc or as an elliptical object. Discs are thereby commonly assumed to be perfectly circular and oriented perpendicular to their host halos' angular momentum, while ellipticals are assumed to

have the same projected 2D shape and orientation as their host halo [29,30]. While assuming that all galaxies are discs, [31] added more realism to the IA modeling by introducing a disc thickness as well as a misalignment between the disc and their host halos' angular momentum, as suggested by hydrodynamic simulations [32]. This misalignment strongly reduced the predicted amplitude of the IA two-point statistics, bringing it in agreement with COSMOS-17 observations. Heymans *et al.* [33] further advanced the semianalytic IA modeling by considering mixed populations of discs and ellipticals in their simulation, while applying a galaxy-halo misalignment only to the disc population. Okumura and Jing [34], Okumura *et al.* [35] found that a misalignment between ellipticals and their host halo is needed in order to reproduce the observed alignment signal of luminous red galaxies (hereafter referred to as LRGs) in the Sloan digital sky survey (hereafter referred to as SDSS). These different semianalytic IA models only considered central galaxies, for which information on halo shape and angular momenta could be obtained from the underlying dark matter simulation. Joachimi *et al.* [[36,37] hereafter jointly referred to as J13] were the first to add satellite galaxies to the semianalytic IA modeling, using constraints on the radial alignment of satellites with respect to their host halos center from a hydrodynamic simulation [38]. Considering both, elliptical as well as disc galaxies, J13 applied their IA model on galaxies from a semianalytic model of galaxy formation imposed on the Millennium Simulation, which exceeded the N -body simulations used in previous works in resolution and volume. They showed that variations of the model parameters controlling the disc thickness and the galaxy-halo misalignment have a significant impact on the predicted IA contamination in the lensing signal. These authors further pointed out that the ellipticity distribution for late-type galaxies in their simulation does not reproduce the observed lack of circular face-on disc galaxies. A more detailed overview on semianalytic IA models can be found in [5]. More recently, [39] applied the model of J13 on a catalog of galaxies from a semianalytic model of galaxy formation that was run on a simulation from the Elucid project, which matched the millennium simulation in volume but exceeds its resolution significantly. In contrast to previous works, this IA simulation included not only intrinsic galaxy ellipticities, but in addition, gravitational shear derived from ray tracing, which allowed for direct predictions of the IA contributions to the lensing signal from the Kilo-Degree Survey (KiDS) and the Deep Lens Survey.

Overall, these different works predicted small but significant contributions of the IA to future lensing surveys. However, these predictions may be affected by different shortcomings in the IA implementation, which we aim to address in this work with the following three steps: (1) We use a new model for the intrinsic galaxy shapes, which reproduces the observed galaxy axis ratio distribution from

the COSMOS survey over wide ranges of redshifts, galaxy luminosities, and colors, accounting for the lack of circular objects; (2) we calibrate the semianalytic IA model for the first time against observational constraints from the BOSS LOWZ survey, provided by Singh and Mandelbaum [[21] hereafter referred to as SM16], taking into account the luminosity dependence of the observed signal by introducing a luminosity dependence in the galaxy-halo misalignment for satellite galaxies; (3) we run this new IA model on the light-cone output of the MICE Grand Challenge simulation [40–42], which provides lensing information together with mock galaxies generated with a hybrid approach of halo occupation distribution modeling and halo abundance matching that was calibrated to match observational constraints on galaxy luminosity and color distributions as well as the galaxy clustering. The MICE light-cone covers one octant of the sky and reaches up to redshift $z = 1.4$, which allows us to create the largest IA simulation produced so far.

We use this simulation for a detailed investigation of the accuracy of two analytical IA models that are applied in current cosmological weak lensing analyses: the nonlinear alignment (NLA) model [10,13,15,43] and the tidal alignment and tidal torquing (TATT) model [9]. We therefore compare these models with measurements in MICE over wide ranges of scales, redshifts, galaxy luminosities, and colors. We further compare constraints on the model parameters derived from the simulation against observational constraints in luminosity and redshift ranges in which the simulation was not calibrated. Lastly, we construct a mock sample resembling Metacalibration [44], the sample used in the analysis of the first three years of data from the Dark Energy Survey (DES), in order to predict the IA contamination in current observations.

The paper is organized as follows. In Sec. II, we introduce the different two-point statistics used in this work together with the two analytical IA models, NLA and TATT. Section III describes the MICE simulation, the spectroscopic mock BOSS LOWZ, and the photometric DES-like samples constructed from the MICE galaxy catalog as well as the COSMOS data that was used in the calibration of the galaxy shapes in MICE. Our method for modeling these shapes is described and validated in Sec. IV, while the modeling of galaxy orientations is described and validated in Sec. V. In Sec. VI, we compare IA two-point statistics measured in MICE using true redshifts against predictions from the NLA and TATT models. In Sec. VII we study the IA contribution to the weak lensing signal in a DES-like photometric sample, as predicted by our simulation. We finally summarize and discuss our findings in Sec. VIII.

II. CORRELATION FUNCTIONS

The two-point correlation function of the galaxy shear is the main probe of lensing surveys and has further been used

for the direct detection of IA in spectroscopic data sets. We therefore focus on this type of statistic for the calibration of the IA signal in MICE and for deriving predictions for the IA contamination in weak lensing observations from the simulation.

Before introducing the specific shear correlations used in this work, let us define the shear itself. In weak lensing studies, galaxies are approximated as 2D ellipses. The shapes and orientations of these ellipses are fully described by the shear, which is commonly defined as a complex spin-2 vector $\gamma = \gamma_1 + i\gamma_2 = \epsilon \exp(i2\phi)$. The galaxy ellipticity $\epsilon = (1 - q_{2D})/(1 + q_{2D})$ is defined via the 2D axis ratio $q_{2D} = B_{2D}/A_{2D}$, where A_{2D} and B_{2D} are the absolute value of the major and minor axis vectors of the ellipse respectively. The galaxy orientation angle ϕ is defined as the angle between one of the two principle axis and an arbitrary reference axis, as we will specify later on.

A. Definitions and estimators

1. Projected galaxy-galaxy, galaxy-shear, and matter-shear correlations (w_{gg}, w_{g+}, w_{m+})

The projected galaxy-shear correlation is commonly used for direct measurements of IA in spectroscopic surveys as it provides a high signal-to-noise ratio compared to the angular shear statistics that are commonly employed in weak lensing cosmology, while being only weakly sensitive to redshift space distortions [e.g., [6,45]]. In our work, we use this statistic to calibrate the IA model in MICE against observational constraints derived from the BOSS LOWZ sample by SM16. In addition, we study the projected galaxy-galaxy correlation to validate the mock BOSS LOWZ samples constructed from MICE that are used for the calibration. When measuring these correlations, we follow SM16 by studying the cross-correlation between a shape sample S , consisting of the galaxies whose IA signal we want to measure and a density sample D , which is used as a tracer for the underlying matter distribution.

The galaxy-galaxy cross-correlation function is defined as $\xi_{gg}(r) \equiv \langle \delta_g^S \delta_g^D \rangle(r)$, where δ_g^S and δ_g^D are the galaxy density contrasts of the shape and density samples, respectively, separated by the distance r , and $\langle \dots \rangle$ is the ensemble average.

We measure this correlation from the data using the estimator from Landy and Szalay [46],

$$\hat{\xi}_{gg} = \frac{(S - R_S)(D - R_D)}{R_S R_D} = \frac{SD - DR_S - R_D S + R_D R_S}{R_S R_D}. \quad (1)$$

Each term in the numerator and denominator on the right-hand side of this equation stands for the counts of galaxy pairs that are separated by r . R_S and R_D are thereby samples of random points that are constructed to follow the radial probability distribution $N(d)$ of the S and D samples,

respectively, where d is the comoving distance from the observer. We smooth the $N(d)$ distribution over $20h^{-1}$ Mpc with a top-hat window function to reduce the impact of cosmic variance and tested that reducing the window size to $10h^{-1}$ Mpc has only a negligible impact on the signal compared to the estimated errors on the signal.

Analogously to the galaxy-galaxy correlation, one can define the galaxy-shear correlation as $\xi_{g+/\times}(r) = \langle \delta^D \gamma_{+/\times} \rangle(\mathbf{r})$. The shear is here defined specifically for each δ^D – γ pair considered in the average $\langle \dots \rangle$ such that the orientation angle is the angle between the galaxies' major axis and the distance vector \mathbf{r} ; i.e., $\phi' = \phi - \phi_r$. In this coordinate system, the shear components are denoted as $\gamma = \gamma_+ + i\gamma_\times$. Radial ($\phi' = 0$) and tangential ($\phi' = \pi/2$) alignment then lead to $\gamma_+ = 1$ and $\gamma_+ = -1$, respectively, with $\gamma_\times = 0$. An alignment of $\phi' = \pi/4$ and $\phi' = -\pi/4$ lead to $\gamma_\times = 1$ and $\gamma_\times = -1$, respectively, with $\gamma_+ = 0$. Following SM16, we focus our analysis on ξ_{g+} , which we measure using a variation of Eq. (1) given by Mandelbaum *et al.* [19],

$$\hat{\xi}_{g+} = \frac{S_+(D - R_D)}{R_S R_D} = \frac{S_+ D - S_+ R_D}{R_S R_D}, \quad (2)$$

with

$$S_+ X = \sum_{i,j} \gamma_+(i|j), \quad (3)$$

where $\gamma_+(i|j) = \text{Re}[\gamma \exp\{-i2\phi_r^{ij}\}]$ is the (+) component of the shear of a galaxy i in sample S , defined with respect to the vector \mathbf{r} pointing to position j in sample X , where ϕ_r^{ij} is the orientation angle of \mathbf{r} at the position i and X refers to either D or R_D .

So far, we introduced ξ_{gg} and ξ_{g+} (jointly referred to ξ_{gx} in the following) as isotropic quantities that are averaged over all orientations of \mathbf{r} . In order to obtain the projected correlations, we measure ξ_{gx} first as a two-dimensional quantity by separating the distance vector $\mathbf{r} = \mathbf{r}_2 - \mathbf{r}_1$ between two points at position \mathbf{r}_1 and \mathbf{r}_2 into a line-of-sight and a transverse (or projected) component. The line-of-sight vector is thereby defined as $\mathbf{n} \equiv (\mathbf{r}_1 + \mathbf{r}_2)/2$. The line-of-sight and transverse components are then obtained as $r_\Pi = \mathbf{r} \cdot \hat{\mathbf{n}}$ and $r_p = (r_\Pi^2 - r^2)^{1/2}$, respectively. For the measurements, we follow SM16 by using 25 logarithmic bins in the interval $0.1 < |r_p| < 200 h^{-1}$ Mpc and 20 linear bins in the interval $0 < |\Pi| < 60 h^{-1}$ Mpc. The projected correlation is then given by

$$w_{gx}(r_p) = \int_{-\Pi_{\max}}^{\Pi_{\max}} \xi_{gx}(r_p, \Pi) d\Pi, \quad (4)$$

where w_{gx} stands for w_{gg} and w_{g+} . Note that the projected matter-shear correlation w_{m+} , which we investigate in Sec. VI, is defined analogously to w_{g+} , while the density sample in Eq. (2) is replaced by a random subsample of the dark matter particle distribution in the simulation.

Errors on the measurements of w_{gg} , w_{g+} , and w_{m+} are estimated using jackknife resampling. The MICE octant is therefore split into $N_{JK} = 88$ angular subregions, which are defined as healpix pixels with $N_{\text{side}} = 8$ (see Fig. 26). The covariance is then estimated as

$$C_{ij}^{JK} = (N_{JK} - 1) \langle \Delta_i \Delta_j \rangle, \quad (5)$$

with $\Delta_i = w_i^{JK} - w_i$, where w_i is the projected correlation measured in the r_p bin i on the full area, w_i^{JK} is the same measurement but neglecting one jackknife subregion, and $\langle \dots \rangle$ is the average over the N_{JK} measurements of Δ_i . When measuring the projected correlations, we use the same healpix subregions to organize the data in a one-dimensional tree structure in order to accelerate the search of galaxy pairs that enter the estimators in Eqs. (1) and (2). We have verified that the angular correlations measured by our code match corresponding measurements from the public code TreeCorr¹ [47].

2. Angular shear-shear correlation

The real-space angular shear-shear cross-correlation between galaxy samples in different redshift bins A and B is one of the main observables used for weak lensing tomography in current surveys such as the DES. The shear field gives rise to a pair of two-point correlations that preserve parity invariance, defined as $\xi_{\pm}^{AB} \equiv \langle \gamma^A \gamma^{*B} \rangle$ and $\xi_{\mp}^{AB} \equiv \langle \gamma^A \gamma^B \rangle$, where $\langle \dots \rangle$ is the average over the products of all galaxy pairs that are separated by an angle θ . With the (+/×) decomposition of the complex shear, these correlations can be written as

$$\xi_{\pm}^{AB} = \langle \tilde{\gamma}_+^A \tilde{\gamma}_+^B \rangle \pm \langle \tilde{\gamma}_\times^A \tilde{\gamma}_\times^B \rangle. \quad (6)$$

We define $\tilde{\gamma} \equiv -\gamma$, following the literature convention in weak lensing cosmology, according to which $\tilde{\gamma}_+$ (often denoted as γ_t) = 1 indicates perfect tangential alignment (see Kiessling *et al.* [5] for a discussion of differences between shear definitions in weak lensing and IA studies). We further follow literature conventions for the notations of the correlations ξ_{\pm}^{AB} and ξ_{g+} . Note here that the subscript + has different meanings in both cases. For ξ_{\pm}^{AB} , the + refers to the addition of the × term in Eq. (6), whereas for ξ_{g+} , it refers to the radial shear γ_+ .

We measure ξ_{\pm}^{AB} in our mock DES-like source sample using a similar estimator as in the analysis of DES Y3 data [e.g., [48]] but with significant simplifications, which can be made because of the absence of observational effects in MICE. In detail, the response factor and weight associated to each galaxy's shear are set to unity, while the mean shear of each sample is negligible. This simplified estimator can be written as

¹<https://github.com/tmjarvis/TreeCorr>.

$$\hat{\xi}_{\pm}^{AB}(\theta) = \frac{S_+^A S_+^B \pm S_{\times}^A S_{\times}^B}{S^A S^B}, \quad (7)$$

with

$$S_+^A S_+^B = \sum_{i \neq j} \gamma_+^A(i|j) \gamma_+^B(j|i). \quad (8)$$

$S_{\times}^A S_{\times}^B$ is defined analogously, and $S^A S^B$ is the number of galaxy pairs between the sample A and B that are separated by θ . Note that this estimator does not use pair counts between random samples in the denominator in contrast to the ξ_{g+} estimators. The sums are taken over pairs for which the angular separation is in the range $|\theta - \Delta\theta|$ and $|\theta + \Delta\theta|$. Both ξ_+^{AB} and ξ_-^{AB} are measured using 20 logarithmically spaced angular bins between $2.5'$ and $250'$, using TreeCorr. The data covariance matrix estimate and cosmology inference are described in Sec. VII C.

B. Analytical modeling

1. NLA and TATT models for IA

In weak lensing analyses, the observed shear is described as the superposition of a component induced by gravitational lensing (γ^G) and a component related to the galaxies intrinsic ellipticity (γ^I); i.e., $\gamma = \gamma^G + \gamma^I$. The contribution of the intrinsic shear to the observed shear correlations is most commonly described analytically using the NLA model [13,43] and the more recent TATT model [9]. Both models are based on the assumption that the galaxy alignment is induced by the tidal tensor of the large-scale matter distribution,

$$s_{ij}(\mathbf{k}) = \left(\hat{k}_i \hat{k}_j + \frac{1}{3} \delta_{ij} \right) \delta(k). \quad (9)$$

The TATT model uses a perturbative approach in which the intrinsic galaxy shear is expressed via the tidal tensor as

$$\bar{\gamma}_{ij}^1 \simeq A_1 s_{ij} + A_{1\delta} \delta s_{ij} + A_2 s_{ik} s_{kj}. \quad (10)$$

The free parameters of the model, A_1 , A_2 , and $A_{1\delta}$, are effective parameters that capture the total response of galaxy shape to the corresponding combination of cosmic tidal and density fields. In this framework, A_1 and A_2 capture the direct impact of tidal alignment and tidal torquing, respectively, as well as contributions from any small-scale astrophysical effects that produce the corresponding response. Similarly, $A_{1\delta}$ includes the impact of density weighting—the fact that we observe IA only at the location of galaxies—as well as other potential effects that can change its value from what we would expect if only density weighting contributed. All three of these IA parameters can depend on galaxy redshift, luminosity, and potentially other properties. The NLA model corresponds to the TATT model without

contributions from tidal torquing; i.e., $(A_2, A_{1\delta}) = (0, 0)$. Finally, because we always use the galaxies shape sample, the TATT model can be applied to describe measurements of w_{m+} , even though this statistic correlates with the unbiased matter density field. We note that this statistic would not capture the impact of higher-order biasing and correlations of these bias terms with IA. However, these contributions are expected to be small and are currently not included in TATT implementations applied to weak lensing data (e.g., [1]).

2. Prediction for w_{m+}

One goal of our work is to obtain predictions for the IA model parameters by fitting a model for the projected matter-intrinsic shear correlation w_{m+} against measurements in the MICE simulation. By studying the matter-shear instead of the galaxy shear correlation, we circumvent the modeling of galaxy bias, which would add uncertainties to our analysis. Besides the bias, the gravitational shear γ^G can also thereby be neglected since we can separate it out in the simulation signal. In any case, its effect on w_{m+} would be negligible by construction since the correlations are studied for pairs with line-of-sight distances $|r_{\parallel}| < 60 h^{-1}$ Mpc over which gravitational lensing contributions should be weak.

We model w_{m+} using a Hankel transformation of the position-intrinsic galaxy shear power spectrum and the Limber approximation

$$w_{m+} = - \int_0^{\infty} \frac{dk_{\perp} k_{\perp}}{2\pi} J_2(k_{\perp} r_p) P_{mI}(k_{\perp} r_p), \quad (11)$$

where J_2 is the second-order Bessel function of the first kind. We compute this transformation by using the code Fast-PT² [49,50]. The matter position-intrinsic galaxy shear power spectrum $P_{mI} = \langle \delta_m \gamma^I \rangle$ is thereby set by the intrinsic alignment parameters as detailed in Blazek *et al.* [9].

3. Prediction for ξ_{\pm}

The modeling of the ξ_{\pm} measurements in our mock DES-like catalog in MICE is more complex than in the case of w_{m+} since we now need to take into account the gravitational as well as the intrinsic component for the observed shear, which are superposed as $\gamma_{\text{obs}} = \gamma^G + \gamma^I$. Inserting this superposition into the definition of the shear-shear correlation between two redshift bins A and B leads to the emergence of several terms in ξ_{\pm} ,

$$\xi_{\text{obs}}^{AB} = \xi_{GG}^{AB} + \xi_{GI}^{AB} + \xi_{IG}^{AB} + \xi_{II}^{AB}. \quad (12)$$

Observationally, these terms cannot be separated from each other, and hence, they need to be modeled when extracting

²<https://github.com/JoeMcEwen/FAST-PT>.

cosmological information from the measurements. However, the MICE simulation allows us to measure each of these terms separately to investigate their contribution to the observed signal in mock surveys constructed from the simulation.

In general, the predictions for the different terms of the angular shear correlation are obtained by

$$\xi_{\pm}^{AB}(\theta) = \sum_{\ell} \frac{2\ell + 1}{2\pi\ell^2(\ell + 1)^2} [G_{\ell,2}^+(\cos\theta) \pm G_{\ell,2}^-(\cos\theta)] C^{AB}(\ell), \quad (13)$$

where $G_{\ell}^{\pm}(x)$ are related to Legendre polynomials $P_{\ell}(x)$ and averaged over angular bins (see, for instance, Krause *et al.* [51]). The GG , II , GI , and IG terms from Eq. (12) enter via the 2D convergence power spectrum, $C^{AB} = C_{GG}^{AB} + C_{GI}^{AB} + C_{IG}^{AB} + C_{II}^{AB}$, and are obtained from the 3D power spectra P again under the Limber approximation as

$$C_{GG}^{AB}(\ell) = \int_0^{\chi_H} d\chi \frac{W^A(\chi)W^B(\chi)}{\chi^2} P_{\delta\delta}\left(\frac{\ell + 1/2}{\chi}, z(\chi)\right), \quad (14)$$

$$C_{GI}^{AB}(\ell) = \int_0^{\chi_H} d\chi \frac{W^A(\chi)n^B(\chi)}{\chi^2} P_{\delta I}\left(\frac{\ell + 1/2}{\chi}, z(\chi)\right), \quad (15)$$

and

$$C_{II}^{AB}(\ell) = \int_0^{\chi_H} d\chi \frac{n^A(\chi)n^B(\chi)}{\chi^2} P_{II}\left(\frac{\ell + 1/2}{\chi}, z(\chi)\right), \quad (16)$$

where $P_{\delta\delta} \equiv \langle \delta\delta \rangle$ is the matter-matter power spectrum, $P_{\delta I} \equiv \langle \delta\gamma^I \rangle$ is the same matter-intrinsic shear power spectrum that enters the w_{m+} prediction in Eq. (11), and $P_{II} \equiv \langle \gamma^I \gamma^I \rangle$ is the intrinsic shear-intrinsic shear power spectrum. Both, $P_{\delta I}$ and P_{II} are obtained from the NLA and the TATT model, as detailed in [9]. Additionally, $n^{A/B}$ is the normalized source galaxy redshift distribution in redshift bins A or B ,

$$W^{A/B}(\chi) = \frac{3H_0^2\Omega_m}{2c^2} \frac{\chi}{a(\chi)} \int_{\chi}^{\chi_H} d\chi' n^{A/B}(z(\chi')) \frac{dz \chi' - \chi}{d\chi' \chi'} \quad (17)$$

is the lensing efficiency kernel, χ is the comoving distance, χ_H is the comoving distance at the horizon, a is the scale factor, H_0 is the Hubble constant, and Ω_m is the matter density.

III. DATA

A. COSMOS

We use observed galaxy magnitudes, redshifts, and shapes from the COSMOS survey to calibrate the color cut and the parameters of the galaxy axes ratio distribution in our IA model. These galaxy properties are obtained from

two public catalogs, the COSMOS2015³ [52] and the Advanced Camera for Surveys General Catalog [ACS-GC,⁴ [53]]. In the following, we briefly described the main properties of these data sets. Details on quality cuts and the matching between both catalogs are described in [54]. The COSMOS2015 catalog comprises photometry in 30 bands and provides redshift estimates, which were derived by fitting templates of spectral energy distributions to the photometric data [55,56]. We discard objects which are classified as (i) residing in regions flagged as “bad” (ii) saturated, and (iii) not classified as galaxies. After these cuts, the sample contains 521,935 objects, which are used to calibrate the color cut employed in our IA model.

In order to constrain the galaxy shape parameters as a function of redshift, we further impose the recommended cuts on the 3σ limiting AB magnitudes in the near-infrared K_s -band of 24.0 and 24.7 in the deep and ultra-deep fields, respectively [52]. The ACS-GC is based on Hubble Space Telescope (HST) imaging in the optical red I_{AB} broad band filter F814W. The absence of atmospheric distortions allows for an excellent image resolution, which is mainly limited by the width of the HST point spread function (PSF) of 0.085” in the F814W filter and the pixel scale of 0.03”. Sources were detected using the GALAPAGOS software [57]. Galaxy shapes are described by the two-dimensional major over minor axes ratios q_{2D} , which are derived from fits of a single Sérsic model and corrected for PSF distortions. We select objects from the catalog that were classified as galaxies with good fits to the Sérsic profile. After applying the quality cuts, the two catalogs are matched based on galaxy positions and magnitudes as described in Hoffmann *et al.* [54]. The final matched catalog contains 98,604 objects.

B. MICE

The MICE Grand Challenge (MICE-GC) simulation [42] is a large N -body run that evolved 4096³ particles in a volume of $(3072 h^{-1} \text{ Mpc})^3$ using the GADGET-2 code [58]. It assumes a flat Λ CDM cosmology with $\Omega_m = 0.25$, $\Omega_{\Lambda} = 0.75$, $\Omega_b = 0.044$, $n_s = 0.95$, $\sigma_8 = 0.8$, and $h = 0.7$. This results in a particle mass of $2.93 \times 10^{10} h^{-1} M_{\odot}$. The initial conditions were generated at $z_i = 100$ using the Zel’dovich approximation and a linear power spectrum generated with CAMB.⁵

The dark-matter light-cone is decomposed into a set of concentric all-sky spherical shells of a given width Δ_r around the observer, following the approach introduced in Fosalba *et al.* [59] [see also [41]]. Given the size of the simulation box, the resulting light-cone outputs show

³<https://www.eso.org/qi/>.

⁴vizier.u-strasbg.fr/viz-bin/VizieR-3?-source=J/ApJS/200/9/acs-gc.

⁵<http://camb.info>.

negligible repetition along any line of sight up to $z = 1.4$. A set of 265 maps of the projected mass density field with $\Delta_r = 35$ megayears in look-back time, and angular healpix resolution $N_{\text{side}} = 8192$ (i.e., 0.43 arcmin pixels) were used to discretize the light-cone volume. These maps were then used to derive the all-sky convergence field κ in the Born approximation by integrating them along the line of sight weighted by the appropriate lensing kernel (see [59] for details). The convergence was transformed to harmonic space, where a simple relation to the shear field holds (for which the B mode exactly vanishes), and transformed back to angular space to obtain the (γ_1, γ_2) components of the shear field. In this way, discretized 3D lensing properties (kappa and shear) were produced across the 3D volume covered by the light cone.

Halos in the light-cone were identified using the friends-of-friends (FoF) algorithm with linking length $b = 0.2$ down to the limit of two particles per halo [40]. Following Carretero *et al.* [60], a combination of halo occupation distribution (HOD) and subhalo abundance matching (SHAM) techniques were then implemented to populate halos with galaxies in one octant of the light cone, covering 5156.6 deg². Galaxy positions, velocities, luminosities, and colors were thereby assigned, such that the catalog reproduces SDSS observations of the luminosity function, the color-magnitude distribution, and the clustering as a function of color and luminosity [61,62]. Spectral energy distributions (SEDs) were then assigned to the galaxies resampling from the COSMOS catalog of [56] galaxies with compatible luminosity and (g-r) color at the given redshift. Once the SEDs are assigned, magnitudes can be computed in any desired filter. In particular, DES griz magnitudes are generated by convolving the SEDs with the DES pass bands.

In order to reproduce with high fidelity the distribution of colors and magnitudes of the DES Year 3 (hereafter Y3) data, we remap the MICE photometry into the observed photometry using an N -dimensional probability density transfer method [63], which preserves the correlation among colors. Once we have remapped the photometry (i.e., distributions of magnitudes and colors) to the one of DES Y3, we compute photometric redshift estimates using the directional neighborhood fitting [DNF, [64]] training-based algorithm. DNF is one of the algorithms used to compute photometric redshifts in DES, albeit not the default one for the source sample. As a training sample for DNF, we consider the same sample used to run DNF on the Y3 data, which is a compilation of spectra from spectroscopic surveys that overlap with the DES footprint (see [65] for details). We will use the remapped photometry and the DNF photometric redshifts in Sec. III E.

1. Halo orientations and angular momenta

The orientations and angular momenta of the FoF halos are main components of our IA model. The orientations

are obtained from the eigenvectors of the reduced moment of inertia

$$I_{i,j} = \frac{1}{N_p} \sum_n \frac{r_{n,i} r_{n,j}}{r_n^2}, \quad (18)$$

where N_p is the number of FoF particles, $r_{n,i}$ are the components of the 3D position vector of the n th particle with respect to the FoF center of mass, and $r_n = \sqrt{r_{n,1}^2 + r_{n,2}^2 + r_{n,3}^2}$ is the particle distance to that center. The angular momentum vectors are given by

$$\mathbf{J} = \sum_n \mathbf{r}_n \times \mathbf{v}_n, \quad (19)$$

where \mathbf{v}_n is the 3D velocity vector of the n th particle, defined with respect to the average velocity vector of all halo particles.

The orientations and angular momenta were measured for FoF groups with down to 10 particles. Using such low numbers of particles can be problematic since noise in the measurements could decrease the halo alignment to a degree that inhibits the induction of a galaxy alignment signal that is sufficiently high to match observational constraints. We therefore investigate the impact of noise on the alignment of halo orientations and angular momenta in Appendix A. For that purpose, we compute these quantities from subsets of random particles of massive halos in MICE and measure a 3D alignment statistics for different subset sizes. We find that even with 10 particles, we are still able to detect a clear signal, although with a significantly decreased amplitude. The dependence of noise in the halo orientations and angular momenta on the number of halo particles will affect the mass dependence of the halo alignment and therefore potentially also the luminosity dependence of the galaxy alignment in the simulation. However, in Sec. V, we argue that we can compensate for such systematic effects when calibrating the galaxy-halo misalignment as a function of galaxy luminosity.

Note further that the FoF particle positions have not been stored in MICE for halos with less than 10 particles, while the HOD model uses halos containing as few as two particles. The 10 particle limit therefore imposes a luminosity cut in the simulation, which we discuss in Appendix B.

A common alternative to the reduced moment of inertia is the standard moment of inertia, which is defined as in Eq. (18), but with $r_n = 1$ in the denominator. By using the reduced instead of the standard moment of inertia, we hence assign more weight to the inner regions of the halos when measuring their orientations. This choice is motivated by the assumption that the central galaxy orientation should be more closely related to the orientation of the host halo

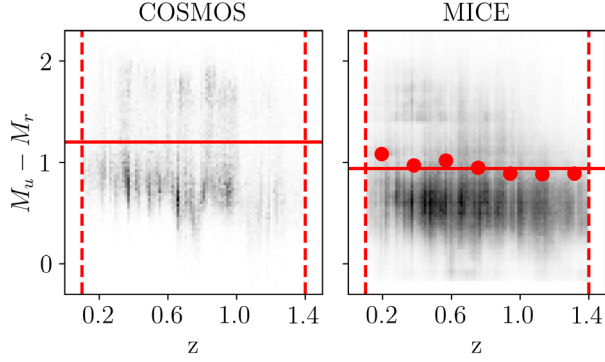


FIG. 1. Absolute rest frame color index versus redshift for galaxies with $m_i < 24$ in COSMOS and MICE. Horizontal solid lines mark the redshift independent cuts used for selecting red and blue subsamples. Dots in the right panel indicate the color cuts in MICE that would reproduce the fraction of red and blue galaxies in COSMOS in different redshift bins.

center than to the orientation of the host halos’ outer regions. Furthermore, FoF particles in the outer regions are more likely to be spuriously linked by the FoF algorithm [e.g., [66]], which may bias the measured orientations. The halo properties measured for this work are part of a public halo catalog that has been presented by Gonzalez *et al.* [67].

C. Color cuts

Observations have shown that the shapes as well as the intrinsic alignment signal depend strongly on galaxy color [e.g., [4,68]]. We incorporate such a color dependence in our model by using different model parameters for red and blue galaxies. The color type is set by a cut in the $u - r \equiv M_u - M_r$ color index, where M_u and M_r refer to the absolute rest frame magnitudes in the CFHT u -band and the Subaru r -band, respectively. We infer the value of this cut by comparing the $u - r$ distributions from MICE and COSMOS in Fig. 1, focusing on galaxies within the redshift and apparent i -band magnitude range covered by MICE; i.e., $0.1 < z < 1.4$ and $m_i < 24$.⁶ We find that a cut at $u - r = 1.2$, shown as horizontal solid line in the left panel of Fig. 1, separates the red and the blue sequences in COSMOS reasonably well at all considered redshifts. The global fraction of blue galaxies in COSMOS defined by this cut is $f_{\text{blue}} = 0.69$. We adjust this cut in the MICE simulation to $u - r = 0.94$ to obtain the same global fraction of blue galaxies, as shown in the right panel of Fig. 1. The red dots indicate the color cut that would reproduce the exact fraction of blue galaxies from

⁶The fluctuations in the redshift distribution, noticeable as vertical stripes in Fig. 1, result from cosmic variance. This variance is expected to be high since the data used for this figure was sampled in narrow light cones of a few square degree in COSMOS as well as in MICE.

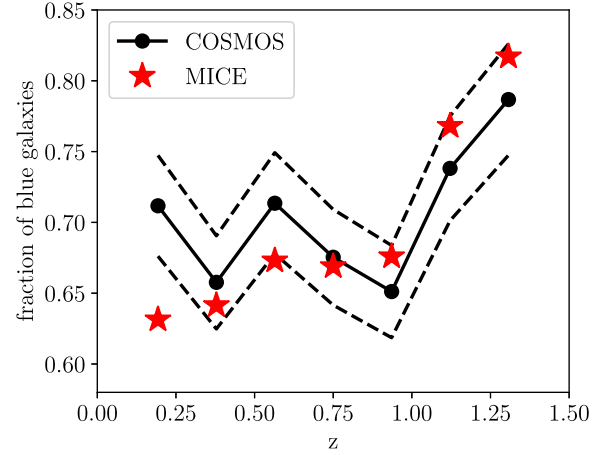


FIG. 2. Fraction of blue galaxies in MICE and COSMOS, selected by the redshift independent color cuts, shown in Fig. 1. The dashed lines mark $\pm 5\%$ deviations from the COSMOS data.

COSMOS in different redshift bins. We find that these redshift dependent cuts lie close to the globally defined cut, which confirms that using a redshift independent cut in MICE is an appropriate choice. As an additional validation, we compare the fractions of blue galaxies in the redshift bins to results in COSMOS in Fig. 2. The blue fractions in MICE lie within 5% of the COSMOS results, except for the lowest redshift bins at $z \simeq 0.2$, where we find a $\simeq 10\%$ deviation.

Note here that a simple color cut does not separate morphological types very well, in particular, because a significant fraction of disc galaxies is red due to dust extinction when seen edge on [e.g., [54,69]]. A more robust selection of morphological types based on photometric properties could be done using a color-color cut, based on two different color indices [e.g., [37]]. However, it is less obvious how to adjust such a color-color selection in the simulation to match the relative abundance of the different morphological types in an observational reference sample. For the sake of simplicity, we therefore proceed using a simple color-cut, leaving more sophisticated cuts as improvements for future updates of our model.

D. Mock BOSS LOWZ samples

For the calibration of our IA model against observed IA statistics of LRGs from the BOSS LOWZ survey from SM16, we construct a mock LOWZ catalog from the MICE simulation. We therefore select galaxies from MICE in the redshift range analyzed by SM16 ($0.16 < z < 0.36$) and apply the LOWZ selection in color-magnitude space, given by

$$\begin{aligned}
 m_r &< 13.5 + c_{\parallel}/0.3 + \Delta m_r \\
 16.0 &< m_r < 19.6 + \Delta m_r \\
 |c_{\perp}| &< 0.2 \\
 0.16 &< z < 0.36,
 \end{aligned} \tag{20}$$

TABLE I. Characteristics of the luminosity subsample from the mock LOWZ catalog constructed from MICE. The columns (from second left to right) show the minimum, maximum, and mean values of the absolute rest-frame SDSS r -band magnitude (M_r), the mean redshifts, and the number of galaxies for each subsample.

Sample	M_r^{\min}	M_r^{\max}	$\langle M_r \rangle$	$\langle z \rangle$	N_g
L1	-23.61	-22.21	-22.43	0.29	30924
L2	-22.21	-21.98	-22.08	0.28	30923
L3	-21.98	-21.76	-21.87	0.27	30923
L4	-21.76	-19.53	-21.41	0.24	61847

where

$$c_{\parallel} = 0.7(m_g - m_r) + 1.2[(m_r - m_i) - 0.18]$$

$$c_{\perp} = (m_r - m_i) - (m_g - m_r)/4.0 - 0.18, \quad (21)$$

and m_g , m_r , m_i are the apparent magnitudes in the corresponding SDSS broad-band filters.⁷

Δm_r is a constant that is zero in the observational LOWZ selection and adjusted to a value of 0.085 in MICE to obtain the observed galaxy number density of the LOWZ sample.

In order to study the luminosity dependence of the IA signal, we follow SM16 by splitting the mock LOWZ sample into four luminosity subsamples, called L1-L4 (from bright to dim), which are selected as quantiles of the absolute SDSS r -band magnitude distribution, containing 20%, 20%, 20%, and 40% of the objects, respectively. The number of galaxies in each subsample is given in Table I together with the corresponding magnitude ranges, mean magnitudes, and mean redshifts. More details on the selection of the MICE LOWZ sample and its luminosity subsamples are given in Appendix B.

We validate our sample selection by comparing the w_{gg} autocorrelation of the full MICE LOWZ sample and its cross-correlation with the subsamples L1-L4 to the corresponding measurements in BOSS observations from SM16 in Fig. 3. We find that the simulation reproduces the overall scale dependence of the observed w_{gg} signal as well as the relatively weak dependence on luminosity. At scales between $20 < r_p < 40 h^{-1}$ Mpc, the amplitudes for the simulated and the observed samples are in good agreement as well with deviations of $\lesssim 10\%$. At smaller and larger scales, the w_{gg} measurements in MICE are up to $\sim 60\%$ and $\sim 90\%$ below the observations, respectively. For scales

⁷Note that the BOSS target selection is based on model magnitudes [70], while MICE magnitudes were assigned to match the Blanton *et al.* [61] SDSS luminosity function derived from Petrosian magnitudes. However, the latter authors find only a weak change of the luminosity function when using model magnitudes. We therefore do not expect the differences in the magnitude definition to be relevant for the construction of the mock BOSS LOWZ samples.

$r_p \gtrsim 10 h^{-1}$ Mpc, the deviation between observation and simulations are consistent with the 1σ error estimates, while the deviations at small scales are highly significant as the errors are smaller. These small scale deviations are similar for the samples L1-L3, and highest for the dimmest sample L4, which could be related to the overdensity artifact at $z \simeq 0.25$ that is discussed in Appendix B.

When interpreting these deviations, it is important to keep in mind that the MICE HOD-SHAM model has been calibrated against the clustering statistics of the SDSS main sample, which covers lower redshifts and dimmer magnitudes than those probed by the BOSS LOWZ survey [60]. Deviations of the galaxy clustering statistics in our mock LOWZ samples from observational results are therefore not unexpected. Furthermore, the cosmological parameters used to simulate the matter distribution in MICE differ significantly from recent constraints, while we expect these deviations to have a weak effect on the clustering compared to the HOD-SHAM parameters. However, given the implications of these deviations on the IA model calibration that we discuss in Sec. VB, it might be worth trying a more sophisticated mock construction by adjusting the LOWZ cuts in MICE, such that the mock samples match the observed clustering instead of the observed number density.

E. DES-like source sample

In order to predict the IA signal for a galaxy population that approximates a realistic weak lensing sample, we construct a mock tomographic catalog utilizing photometric redshift estimates in MICE. The mock sample resembles the one used in the DES Y3 analysis [METACALIBRATION, [44]] in its overall magnitude and redshift distribution, as well as in constraining power in the cosmological parameter space as described below.

Firstly, we verify in Appendix B that the (nontomographic) magnitude distributions in the r , i , and z DES broad bands from the Y3 data are in good agreement with the distributions of remapped magnitudes in MICE (described in Sec. III B). The resulting MICE DES-like mock contains over 130 million galaxies, which is slightly more than the 100 million galaxies in the DES Y3 catalog but is roughly consistent in number density given the $\sim 25\%$ greater area of the MICE octant compared to DES. Additionally, where cosmology inference is carried out, we adapt the per-galaxy shape noise in order to match the DES Y3 small-scales covariance (see Sec. VII C).

Secondly, we split our mock sample into tomographic bins along the line of sight using photometric redshifts estimated for MICE galaxies with the DNF algorithm described in Sec. III B. We sort galaxies into four bins defined by hard nominal edges that match DES Y1: [0.2, 0.43, 0.63, 0.90, 1.30] [71]. While this procedure is different than the methodology employed in DES Y3, based on self-organizing maps (SOMPZ) [72], it suffices for our goal to create a set of realistic redshift distributions

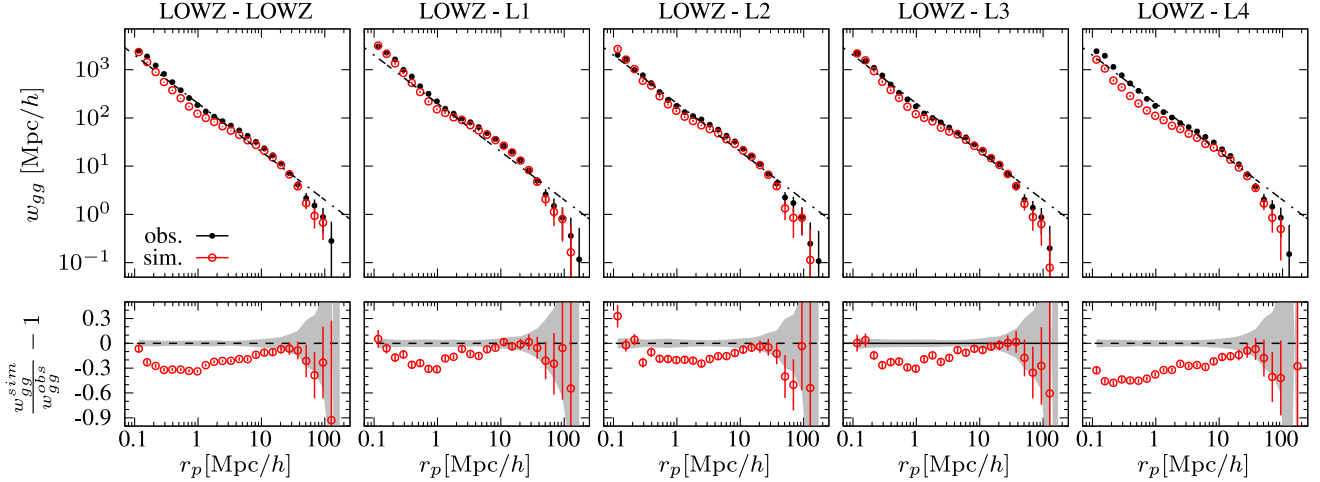


FIG. 3. Top: Projected galaxy correlation functions from the BOSS LOWZ survey (SM16) and a mock catalog constructed from the MICE simulation (black dots and red open circles, respectively). The left panel shows the autocorrelation measured in the full LOWZ sample, and the panels on the right show the cross-correlation between the full LOWZ sample and four luminosity subsamples L1-L4 (from bright to dim; see Sec. III D for details on the sample selection). Error bars show estimates of the 1σ uncertainty on the measurements. The dashed-dotted black lines shows the same $200 r_p^{-1}$ power law in all panels as a visual guidance for comparing the variation in the amplitude across different samples. Bottom: Relative deviations between measurements in observations and in MICE. The gray shaded areas indicate the 1σ errors on the observations.

that approximate a DES selection. We show histograms of the true redshifts of the galaxies binned via DNF point-estimates in Fig. 4, with an overall mean redshift of $z = 0.6$, along with the binned DES Y3 distributions [72] for a visual comparison. We note that the MICE redshift distributions are generally narrower and peak higher redshifts than their DES Y3 counterparts. The methodological differences between MICE and DES Y3 redshifts exist for practical purposes and imply that the testing presented here should be taken as an additional piece of evidence that the IA modeling in DES Y3 is sound, though not as a final proof.

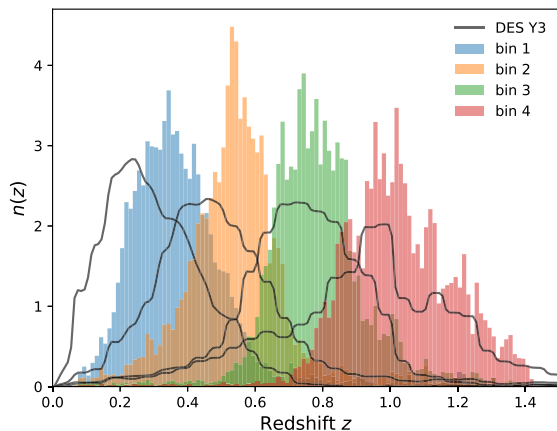


FIG. 4. Arbitrarily normalized redshift distribution of the DES-like MICE source sample (solid histograms) and real DES Y3 data (black lines). Redshift point estimates in MICE are obtained with DNF and qualitatively resemble the $n(z)$ distributions in DES Y3 (see text for further details).

We find that a significant fraction of central galaxies are defined as blue by the color cut used in our modeling (see Table II). Since the orientations of blue galaxies are highly randomized in our model (see Sec. V), we can already expect from this finding that the IA signal in the DES-like samples predicted by our model will be weak, which is indeed the case (see Sec. VII). A more detailed discussion on the galaxy color distribution in the DES-like samples can be found in Appendix B.

F. Volume limited samples

We construct two sets of volume-limited color samples. The first set is used to derive predictions for the two-point IA statistics up to high redshifts where observational constraints are currently not available. It covers three redshift bins that are centered around $z = 0.2$, $z = 0.4$, and $z = 0.6$ and have a width of $\Delta z = 0.2$. Galaxies in each redshift bin are separated into six bins by their absolute rest frame SDSS r -band magnitude (M_r), which have a width of $\Delta M_r = 1.0$. The faint limit of these magnitude samples is set to $M_r < -20$ to ensure that host halo shape

TABLE II. Fraction of blue galaxies in the DES-like from MICE samples, defined by our $u - r = 0.94$ color cut.

z bin	Centrals	Satellites	Centrals + Satellites
1	0.526	0.386	0.467
2	0.583	0.332	0.467
3	0.589	0.298	0.488
4	0.667	0.358	0.594

measurements are available for all central galaxies in the sample (see Appendix B). Each of the resulting volume limited samples is further split into a red and a blue subsample at the same $u - r = 0.94$ color cut, which we use in our IA model (Sec. III C). The selection of the resulting 36 samples is illustrated Fig. 25.

A second set of volume-limited color samples is constructed to calibrate the parameters of our shape model against COSMOS observations. Each of these samples has a width of $\Delta z = 0.2$ and $\Delta M_r = 1$ in redshift and absolute Subaru r -band magnitude, respectively. The samples are equally spaced on a regular grid in the $z - M_r$ space with an overlap of $\Delta z/2$ and $\Delta M_r/2$. This overlap allows for an increased sampling resolution while keeping the number of galaxies per sample large enough to allow for statistically meaningful measurement of the 2D axis ratio distribution over a wide range in magnitude and redshift. We discard samples that contain less than 100 galaxies, which leads to 115 and 196 samples for red and blue galaxies, respectively. The positions of these samples in magnitude-redshift space are shown as dots in the right panels of Fig. 5, where each dot's color indicates the number of galaxies in the corresponding sample. We use 10 samples from the second set as examples to validate if the distribution of galaxy axis ratios in the final MICE IA simulation matches the reference observations from COSMOS. The areas spanned in the magnitude-redshift space by these example samples are shown in Fig. 24. Note that red and blue subsamples are selected in MICE by the same cut at $u - r = 0.94$ used in the first set of samples, while we cut the COSMOS samples at $u - r = 1.2$ as explained in Sec. III C.

IV. MODELING GALAXY SHAPES

Our model for galaxy shapes is based on the assumption that each galaxy's shape can be approximated as a 3D ellipsoid whose shape is fully described by two of the three axis ratios

$$q_{3D} \equiv \frac{B_{3D}}{A_{3D}}, \quad r_{3D} \equiv \frac{C_{3D}}{B_{3D}}, \quad s_{3D} \equiv \frac{C_{3D}}{A_{3D}}, \quad (22)$$

where A_{3D} , B_{3D} , C_{3D} are the 3D major, intermediate, and minor axis, respectively. This modeling choice is motivated by findings reported in the literature, which show that randomly oriented populations of such 3D ellipsoids can lead to distributions of projected 2D axes ratios,

$$q_{2D} \equiv B_{2D}/A_{2D}, \quad (23)$$

which match those from observed ensembles of early- as well as late-type galaxies with high accuracy [e.g., [73–77]]. In particular, this model describes successfully the lack of circular face-on galaxies (i.e., $q_{2D} \simeq 1$) found in observations. Achieving such a match was shown to be problematic in previous work in which discs were modeled as flat coinlike cylinders [36]. However, whether this lack is physical, a result of observational limitations or both remains an open question [e.g., [36,78–81]].

Besides the ellipsoidal model for each galaxy's shape, matching the observed 2D axis ratio distribution further requires a model for the distribution of 3D axes ratios. Several models of such distributions have been presented in the literature [see [54], for an overview]. In this work, we employ a simple Gaussian model,

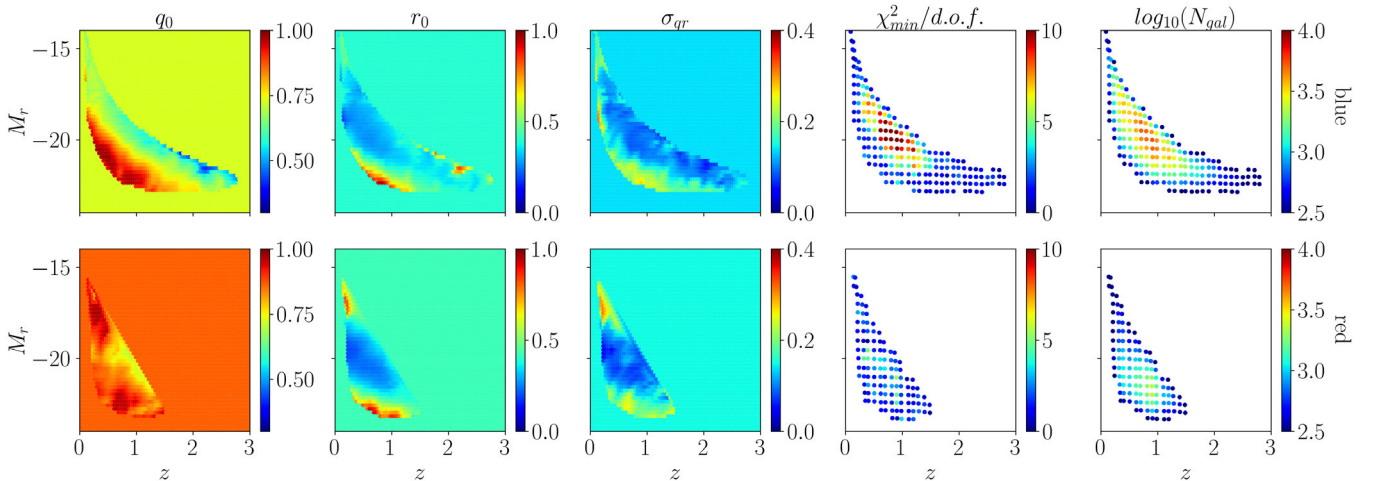


FIG. 5. *Left, central left, central panels*: Interpolated distribution of the parameters in our Gaussian model for the 3D galaxy axis ratio distribution, q_0 , r_0 , and σ_r , given in Eq. (24) as a function of galaxy redshift and absolute r -band magnitude for blue and red galaxies (top and bottom panels respectively). The parameters were derived from the 2D galaxy axis ratio distributions, measured in overlapping volume limited samples in the COSMOS survey (see Sec. IV for details). *Central right panel*: χ^2 per degree of freedom ($d.o.f.$) of the fits to the observed 2D axis ratio distribution for each volume limited sample. *Right panel*: Number of galaxies per volume limited sample. The dots in the right panels are located at the mean redshifts and r -band magnitudes of the volume limited samples.

$$\tilde{P}(q_{3D}, r_{3D}) = \exp\left\{-\frac{1}{2}\left[\left(\frac{q_{3D} - q_0}{\sigma_{qr}}\right)^2 + \left(\frac{r_{3D} - r_0}{\sigma_{qr}}\right)^2\right]\right\}, \quad (24)$$

where q_0 , r_0 , and σ_{qr} are the free model parameters. The normalized truncated distribution is then given by

$$P = \begin{cases} \tilde{P}_{3D}/\mathcal{N} & \text{if } q_{3D}, r_{3D} \in (0, 1] \\ 0 & \text{else} \end{cases} \quad (25)$$

with $\mathcal{N} = \int_0^1 \int_0^1 \tilde{P}_{3D}(q_{3D}, r_{3D}) dr_{3D} dq_{3D}$. This model is motivated by the model proposed by Hoffmann *et al.* [54], which we simplify by assuming the same width σ_{qr} for q_{3D} and r_{3D} to reduce the numbers of free parameters in our simulation.

To model the shape of a specific galaxy in the simulation, we first draw the two 3D axis ratios q_{3D} and r_{3D} randomly from the distribution in Eq. (25). The observed 2D axis ratio is obtained later on by projecting the 3D ellipsoid on a tangential plane that is oriented perpendicular to the observers line of sight, following the methodology presented in J13. Note that this projection requires not only the 3D axis ratios as input, but also each galaxy's 3D orientation. The modeling of the latter is described in Sec. V. An important aspect for producing realistic mock observations is to incorporate the dependence of the galaxy shapes on photometric properties and redshift. We introduce such a dependence in our model by adjusting the parameter vector $\mathbf{p} \equiv (q_0, r_0, \sigma_{qr})$, according to each galaxy's redshift, absolute magnitude, and color before drawing its 3D axes ratios.

A. Parameter calibration

We determine the dependence of the parameter vector \mathbf{p} on redshift and absolute r -band magnitude for a given color (red or blue) from the observed distribution of 2D axes ratios $P(q_{2D})$ in COSMOS. The $P(q_{2D})$ distribution is therefore measured for red and blue galaxies (defined via the $u - r$ color index as detailed in Sec. III C) in the volume limited COSMOS samples that are described as the second set in Sec. III F. For each of these samples, we determine the values of \mathbf{p} for which the corresponding $P(q_{2D})$ prediction fits the observations. We obtain this prediction for a given candidate \mathbf{p} by first generating a set of N 3D ellipsoids, whose 3D axis ratios are drawn randomly from the distribution in Eq. (25). For each 3D ellipsoid in this set, we then compute q_{2D} following J13 while assuming a random 3D orientation. The $P(q_{2D})$ prediction is then measured from the resulting set of N projected 2D axis ratios and compared to the reference measurement from the observed sample. The observed as well as the predicted distributions are thereby measured using the same binning in q_{2D} . The number of bins is adjusted to the number of galaxies in each COSMOS

subsample, following the Freedman–Diaconis rule for optimal binning [82]. We derive the best fit values \mathbf{p} by maximizing the likelihood which is computed from the χ^2 deviation between the predicted and the observed $P(q_{2D})$ distribution. For the measurements, we assume shot-noise errors while neglecting errors on the predictions since those are generated using much higher number of axis ratios (i.e., 1000 points per bin on average). The posterior of the parameter space is estimated using the Markov-Chain-Monte-Carlo algorithm `emcee`⁸ [83] with flat priors in the ranges $0.01 < q_0 < 0.99$, $0.01 < r_0 < 0.99$, and $0.01 < \sigma_{qr} < 0.35$. The upper limit for σ_{qr} is set to an arbitrary value that is chosen to be well above the typical best fit values found for this parameter. We define the best fit parameters as the position of the maxima of the marginalized posterior distribution.

The distribution of the fitted \mathbf{p} components (q_0 , r_0 , σ_{qr}) in the redshift-magnitude plane, interpolated between the positions of the volume limited samples, is shown for red and blue galaxies in the three left panels Fig. 5. The second panel from the right shows the corresponding χ^2 per q_{2D} bin, which correlates with the number of galaxies per sample, shown on the right of Fig. 5. This correlation means that deviations between best fit model and reference measurements become more significant as the shot-noise errors on the measurements decrease. This indicates that our shape model is too simple to capture the details of the observed 2D shape distributions. An improvement on that aspect might be possible by using more flexible extensions for the 3D axis ratio distribution model [e.g., [54]]. However, such an extension would introduce additional parameters in our modeling, while we find the model employed here to be sufficiently accurate for the purpose of this work, as detailed in the following.

B. Shape mock construction and validation

We assign 3D axes ratios to a given galaxy in the simulation by linearly interpolating the constrained values of q_0 , r_0 , and σ_{qr} for red and blue samples at the galaxy's position in the magnitude-redshift space. For galaxies in the simulation that lie outside of the magnitude-redshift range covered by the COSMOS data, we assign the average values of the parameters over all volume limited subsamples within each red and blue sample, shown as homogeneously colored areas in Fig. 5. Note that a more sophisticated extrapolation of the observational constraints is not trivial due to the complex dependence of the parameters on magnitude and redshift. However, in practice, this problem is not relevant as most galaxies used in our analysis lie within the magnitude and redshift ranges covered by COSMOS.

We validate the performance of our model by comparing the $P(q_{2D})$ distributions from MICE against measurements

⁸emcee.readthedocs.io.

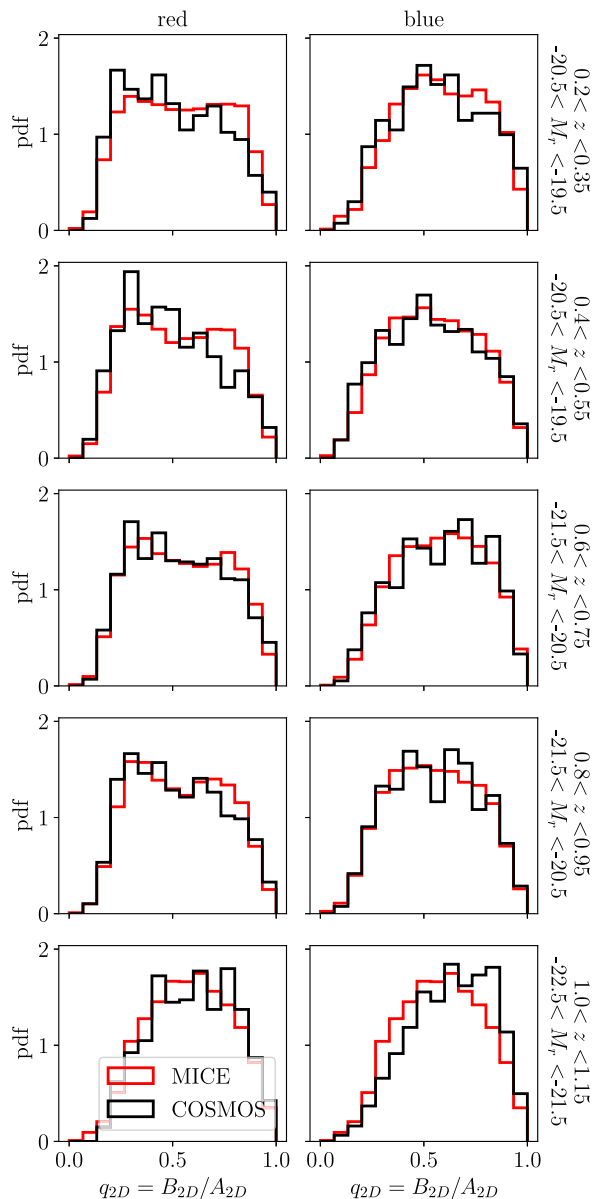


FIG. 6. 2D galaxy axes ratios measured for red and blue galaxies in different volume limited samples. The redshift and absolute Subaru r -band limits of each sample are indicated on the right. Red and black histograms show results from the MICE simulation and COSMOS observations, respectively.

from COSMOS in Fig. 6 for the set of 10 volume limited samples described in Sec. III F and displayed in Fig. 24. We find an overall good agreement between the simulated and observed data. Deviations are most noticeable for the brightest sample of blue galaxies at $z \simeq 1.1$. They may result from the shortcomings of the modeling that we discussed in the previous subsection, from potential inaccuracies in the linear interpolation of the model parameters as well as from differences between the redshift-magnitude distributions of observed and simulated galaxies within a given sample. It is interesting to note that the $P(q_{2D})$

distributions for red and blue galaxies deviate significantly from those expected for discy and elliptical galaxies, respectively. The observed distributions for disc galaxies show typically a plateau in the center (at $q_{2D} \simeq 0.5$) with two kneelike cutoffs on each side. Those for ellipticals have typically the shape of a skew Gaussian distribution with a maximum close to unity and a long tail toward low axis ratios [e.g., [84]]. The reason that the axis ratio distributions of our color subsamples do not follow this expectation may result from the fact that a single color cut does not separate different morphological types very well as detailed in Sec. III C.

V. MODELING GALAXY ORIENTATIONS

We implement 3D galaxy orientations using methodology from Joachimi *et al.* [37], with some modifications. Galaxies are thereby separated into three groups: red centrals, blue centrals, and satellites, where the latter include red as well as blue objects. Red and blue galaxies are selected as described in Sec. III C.

Red centrals have their 3D principle axes aligned with those of their host halo; i.e., $(\hat{A}_{3D}, \hat{B}_{3D}, \hat{C}_{3D})^{\text{gal}} = (\hat{A}_{3D}, \hat{B}_{3D}, \hat{C}_{3D})^{\text{halo}}$. This alignment is based on the assumption that all red galaxies are pressure supported ellipticals whose shape and orientation is set by the same tidal stretching that determines the shape and orientation of the host halo.

Blue centrals are assumed to be rotationally supported discs, whose minor axis is aligned with the angular momentum vector of the host halo, i.e., $\hat{C}_{3D}^{\text{gal}} = \hat{J}_{3D}^{\text{halo}}$, while the major axis \hat{A}_{3D} is oriented randomly on a plane that is perpendicular to the minor axis.

Satellites Red and blue satellites are assumed to have their major axes pointed toward the host halo center, while the minor axis is oriented randomly on a plane that is perpendicular to the major axis. This model assumption is motivated by evidence for a preferred orientation toward the center that has been found in observations as well as simulation. An illustration of the model is shown in Fig. 7. Within the framework of the analytical IA models described in Sec. II, the alignment between central ellipticals and their host halo can be associated with the tidal alignment terms, while the alignment between central discs and the host halo's angular momentum can be associated to the tidal torquing terms. The combined effects of tidal alignment, tidal torquing, and the impact of galaxy density weighting are captured by the parameters A_1 , A_2 , and $A_{1\delta}$.

Note here that our assumption that all blue galaxies are discs and all red galaxies are ellipticals is motivated by the observed correlation between morphological and photometric galaxy properties. However, the simple color cut used in this work may lead to an inaccurate discrimination between the two morphological types, as we discuss in Sec. III C. Future updates of our model may therefore employ more complex photometric cuts to define discs and

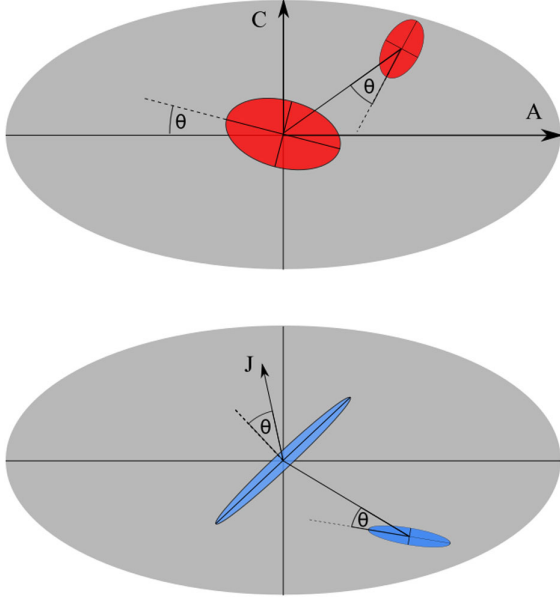


FIG. 7. 2D Illustration of the model used for assigning 3D galaxy orientations in the MICE simulation for red and blue galaxies (top and bottom subfigures, respectively). The major and minor axes of red centrals are aligned with those of their host halo. The minor axis of blue centrals is aligned with the angular momentum vector of the host halo. The major axes of red and blue satellites are pointed toward the halo center. In a subsequent step of the modeling, the orientations are distorted by a random angle θ that depends on galaxy type, magnitude, and color.

ellipticals. For detailed discussions of how the different model assumptions are motivated by observations, hydrodynamic simulations, and analytical models, we refer the reader to the reviews of Joachimi *et al.* [4], Kiessling *et al.* [5], Kirk *et al.* [6], and references therein.

A. Misalignment

Deviations from this simplistic model are accounted for by randomizing the galaxy orientations in a subsequent step. Such a randomization has been shown to be an effective way to calibrate semianalytic IA simulations against observed alignment statistics [e.g., [31,35,37]]. In this work, we randomize the galaxy orientations in 3D before projection along the observers line of sight. This approach allows for extracting constraints on the 3D galaxy alignment from calibrating the model against 2D observations. In addition, it opens up the possibility to calibrate the model against 3D alignment statistics measured at high redshifts in hydrodynamic simulations in future studies. For the randomization, we draw misalignment angles θ from the Mises-Fisher distribution,

$$P(\cos(\theta)) = \frac{1}{2\sigma_{mf}^2 \sinh(\sigma_{mf}^{-2})} \exp\left(\frac{\cos(\theta)}{\sigma_{mf}^2}\right), \quad (26)$$

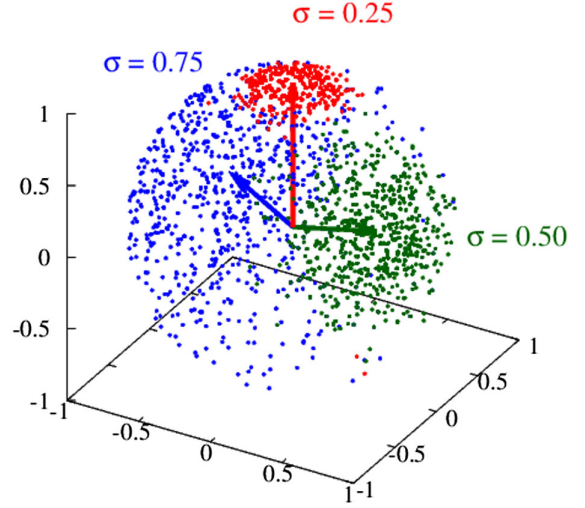


FIG. 8. Mises-Fisher distribution for different misalignment parameters σ_{mf} . Points mark randomized orientations on the surface of a unit sphere with respect of an input vector. The Mises-Fisher distribution is used for randomizing galaxy orientations in our IA model.

where the width σ_{mf} is a free parameter of our model. Higher values of σ_{mf} lead to a higher randomization of the original orientation vector (see Fig. 8) and therefore to a lower alignment signal. Bett [85] showed that in hydrodynamic simulations, the distribution of misalignment angles between the galaxy spin vector and the host halos minor axis is well approximated by Eq. (26). It has therefore been used by Joachimi *et al.* [37] to model the 3D misalignment of the circular discs in their model. In our model, we use Eq. (26) to model the 3D misalignment for all types of galaxies (including discs, ellipticals, centrals, and satellites) with respect to their initial orientations. Assuming that this modeling is valid not only for discs, but also for ellipticals, we are able to successfully reproduce observed alignment statistics of LRG samples that consist mainly of ellipticals (see Sec. V B). However, it would be worthwhile to validate this assumption with measurements of galaxy-halo misalignment of ellipticals from hydrodynamic simulations [similar to those presented, for instance, by [27,86,87]].

Since we model all galaxies as 3D ellipsoids that are in general rotationally asymmetric, we need to randomize their orientations in two directions. We thereby start by randomizing the orientation of the minor and major axes A_{3D} and C_{3D} , using two misalignment angles θ_A and θ_C , which are drawn from the Mises-Fisher distribution with the same value of σ_{mf} for both angles. The randomized orientation vectors \hat{A}_{3D}^r and $\hat{C}_{3D}^{r'}$ are constructed such that $\hat{A}_{3D} \cdot \hat{A}_{3D}^r = \cos(\theta_A)$ and $\hat{C}_{3D} \cdot \hat{C}_{3D}^{r'} = \cos(\theta_C)$. $\hat{C}_{3D}^{r'}$ is thereby a temporary vector that is in general not perpendicular to \hat{A}_{3D}^r . The final randomized minor axis orientation is therefore obtained as $C_{3D}^r = (\hat{A}_{3D}^r \times \hat{C}_{3D}^{r'}) \times \hat{A}_{3D}^r$ and is then normalized to $\hat{C}_{3D}^r = C_{3D}^r / |C_{3D}^r|$. In order

TABLE III. Parameters describing the magnitude dependence of the misalignment parameter σ_{mf} in Eq. (27).

	a	b
Red centrals	0.65	0.0
Red satellites	0.7	-7.7
Blue centrals	2.0	0.0
Blue satellites	2.0	0.0

to control the dependence of the alignment on galaxy magnitude and color, we introduce simple dependencies of σ_{mf} on these properties. We thereby assume a linear relation between σ_{mf} and the absolute r -band magnitude M_r ,

$$\sigma_{mf}(M_r) = a + b \left(\frac{M_r}{M_0} - 1 \right), \quad (27)$$

where a and b are free model parameters, and $M_0 = -22$ is an arbitrarily chosen normalization constant. The color dependence of the alignment is introduced in the model by using different values of a and b for red and blue galaxies, where the colors are defined as described Sec. III C. When adjusting these parameters, we further separate between central and satellite galaxies, which provides control over the scale-dependence of the IA signal in the simulation. The parameters used in our model are summarized in Table III. They are obtained from calibrating the model by hand, as outlined in the next subsection. The final output of the IA model are the two 3D axis ratios q_{3D} and s_{3D} as well as the orientations of the three principle axes for each galaxy in the simulation. In order to compare this output to observations, we project these ellipsoids along the observer's line of sight, who is located at $z = 0.0$ in the MICE light cone, and obtain the intrinsic shear components, as described in Sec. IV.

B. Parameter calibration against observed IA statistics

We calibrate the parameters for controlling the randomization of galaxy orientations, a and b in Eq. (27), for red and blue galaxies separately. For blue galaxies, including centrals as well as satellites, we set $[a, b] = [2, 0]$ such that $\sigma_{mf} = 2$, independent of the galaxy magnitude. The randomized orientations for blue galaxy are consequently close to a uniform distribution on a sphere (see Fig. 8). This choice is motivated by the nondetection of intrinsic alignment for blue galaxies in the surveys WiggleZ, SDSS, DES, and PAUS [17, 18, 20, 88]. However, achieving such a nondetection in the simulation may also be possible with much lower values of σ_{mf} , since the halos' angular momentum alignment is relatively weak compared to the alignment of the halos' principle axes, as we show in Appendix A.

For red galaxies, we adjust a and b such that the simulation reproduces the observed scale and magnitude dependence of the alignment statistics, measured for LRGs

in the BOSS LOWZ sample by SM16. The alignment is thereby quantified with the projected cross-correlation between positions of galaxies in a density sample and the intrinsic shear of galaxies in a shape sample, w_{g+} , as detailed in Sec. II.

Before discussing the calibration in more detail, we show in Fig. 9 how the IA correlation reacts to variations of σ_{mf} for a test sample of galaxies that are brighter than $M_r = -21$ in the redshift range $0.1 < z < 0.3$. When computing the IA correlation, we use the matter distribution of the simulation as the density sample in order to minimize noise on the measurement. The corresponding correlation is hereafter referred to as w_{m+} . In this test case, we set the same σ_{mf} for galaxies of all luminosities and all colors. We find in Fig. 9 that the overall amplitude decreases by roughly a constant factor when increasing the misalignment by increasing σ_{mf} for satellites as well as for centrals from 0.1 to 0.5 (comparing red and yellow lines). When increasing only the misalignment of satellites, we find the signal to decrease only at small scales ($r_p < 5h^{-1}$ Mpc), while it remains unaffected at large scales (comparing red and blue lines). Increasing the misalignment only for centrals on the other hand has an effect on all scales, while the impact is stronger on scales larger than $r_p > 5h^{-1}$ Mpc (comparing red and green lines). In practice, the fact that satellite alignment does not affect the alignment statistics in the simulation at large scales

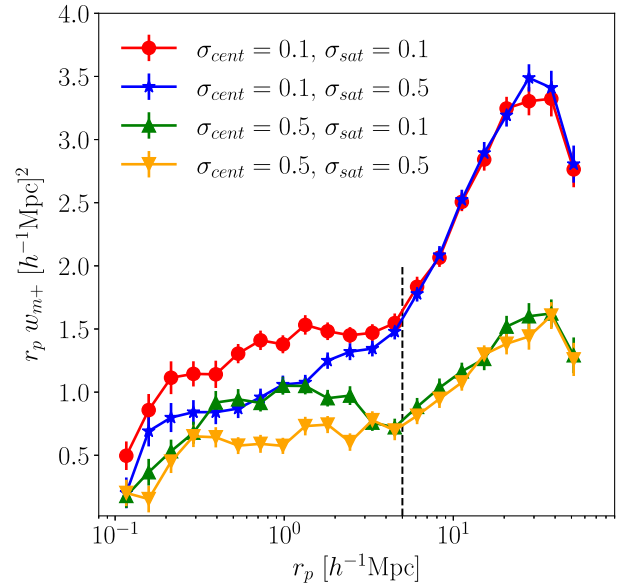


FIG. 9. Projected matter-intrinsic shear correlation w_{m+} for test runs of the semianalytic IA model on a catalog of MICE galaxies with $0.1 < z < 0.3$ and $M_r < -21$, using one misalignment parameter for all centrals (σ_{cent}) and one for all satellites (σ_{sat}), independently from galaxy luminosity and color. Results are shown for different values of σ_{cent} and σ_{sat} . Increasing σ decreases the amplitude of w_{m+} . Misalignment of centrals affects the signal at all scales, while the impact of satellite misalignment is limited to $r_p \lesssim 5 h^{-1}$ Mpc (vertical dashed line).

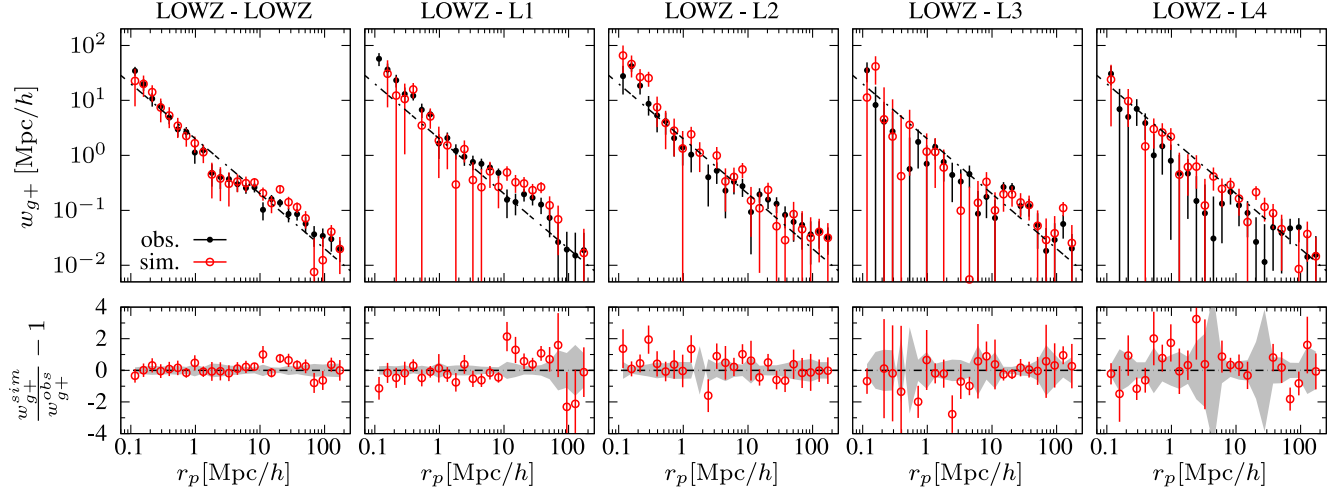


FIG. 10. Similar to Fig. 3, but for the projected galaxy-shear cross-correlation between a density sample and different shape samples. The left panel shows results using the full LOWZ sample as shape as well as density sample. The panels on the right show results based on shapes from the four luminosity subsamples L1-L4, while using the full LOWZ sample as density sample.

simplifies the model calibration, as we can first calibrate σ_{mf} for centrals focusing on the large scales before calibrating the parameters for satellites focusing on small scales.

In order to calibrate the parameters a and b in the $\sigma(M_r)$ relation from Eq. (27), we measure w_{g+} in our mock LOWZ sample (described in Sec. III D), where we take the full sample as density sample and the four luminosity subsamples L1 – L4 as shape samples, following SM16.⁹

As a first step in the calibration, we then set magnitude independent values of σ_{mf} for centrals and satellites for each LOWZ luminosity sample separately. These values are chosen such that χ^2 deviation between w_{g+} measurements in MICE and the observational reference is minimized. We thereby obtain a relation between σ_{mf} and the mean r -band magnitude $\langle M_r \rangle$ of each sample, from which we can infer a first guess of the parameters a and b . Starting from this first guess, we then vary a and b by hand until the simulation matches the observed w_{g+} measurements for the different luminosity samples L1 – L4 simultaneously. Note that this match is quantified purely by eye. In future work, we plan to improve the calibration technique, using quantitative measures for IA model performance and an automated calibration pipeline. Figure 10 shows the comparison between w_{g+} from the calibrated MICE simulation together with the observational reference measurements from SM16. The simulation reproduces the observed dependence of w_{g+} on scale as well as on magnitude as the deviations from the

observations are consistent with the 1σ jackknife error estimates. The errors on the MICE results are overall larger than those on the observations, which can be expected from the smaller area covered by the MICE octant. In addition, differences in the errors can result from differences in the size and geometry of the jackknife samples.

When calibrating σ_{mf} on the different LOWZ luminosity samples, we compensate automatically for systematic effects in the mass dependence of the host halo alignment (see Appendix A), at least within the luminosity and redshift ranges covered by the LOWZ sample. It is not obvious that this compensation also works for magnitudes and redshifts that are not considered in the calibration. However, our results in Sec. VI indicate that this might be the case since the IA amplitudes predicted by MICE for luminosities and redshifts that are not covered by the LOWZ sample are consistent with various observational constraints.

A shortcoming in our calibration based on w_{g+} results from the fact that this statistics is not only sensitive to the alignment, but also to the clustering of galaxies. Since the clustering, quantified by w_{gg} for the MICE LOWZ samples, is predicted to be $\lesssim 30\%$ below the reference observations from BOSS (Fig. 3), we are setting the IA signal in the simulation too high when trying to match the observed w_{g+} signal. However, we expect the error on the w_{g+} amplitude to be significantly smaller than 30% based on the following consideration. At large scales, we can approximate $w_{gg} \propto b_1^2$ and $w_{g+} \propto b_1$, where b_1 is the linear clustering bias. Assuming that the difference in w_{gg} between MICE and BOSS is mainly driven by differences in b_1 , a 30% inaccuracy in b_1^2 would propagate into a 17% inaccuracy on b_1 and hence on w_{g+} . This inaccuracy is well below the dependence of w_{m+} on luminosity, color, and redshift, which we will study later on.

⁹Note that SM16 showed that different shape measurement methods can lead to $\sim\sigma$ variations of the observed signal, which introduces additional uncertainties in our modeling. In this work, we calibrate the simulation against their results based on regaussianized shapes [89,90]. Further note that SM16 apply cuts based on the quality galaxy shape measurements, which we cannot mimic in the construction of mock catalogs from MICE.

Another potential source of bias in our calibration may result from the fact that the galaxy shapes in our simulation are calibrated against observed axis ratio distributions that were derived from Sérsic model fits (Sec. III A). Using a reference distribution based on a different shape measurement method may change the galaxy ellipticity distribution and hence lead to a change in w_{g+} (e.g., SM16). However, since in our simulation the orientations and shapes are calibrated independently, a bias in the ellipticities can be compensated by adjusting the galaxy misalignment, such that w_{g+} still matches the observational constraints.

C. Distribution of misalignment angles

The distribution of misalignment angles between galaxies and their host halos has been investigated in several previous studies. It therefore provides an opportunity to validate our simulation in a way that is independent of the w_{g+} comparison against the BOSS LOWZ constraints, used for the calibration of the simulation parameters. Observational constraints on the distribution of misalignment angles of LRGs have been derived by Okumura and Jing [34] and Okumura *et al.* [35] (jointly referred to as OO9 in the following). Using a methodology similar to the one presented in this work, these authors randomized the orientations of dark matter halos from an N -body simulation such that the simulation reproduces the observed alignment statistics of LRGs in the SDSS. In contrast to our approach of randomizing galaxy orientations in 3D before projection, OO9 randomized the 2D orientations after projection, assuming a Gaussian distribution of misalignment angles with zero mean and a variance σ_ϕ . In order to compare their results to predictions for the LRGs in the mock BOSS LOWZ sample from MICE, we compute the 2D misalignment angles as the difference between the 2D orientation angles before and after randomizing the galaxies in the simulation. We find the variance of the distribution of 2D misalignment angles in the LOWZ sample to be $\sigma_\phi = 32.64^\circ$, which deviates by just $\sim 7\%$ from the $\sim 35^\circ$ degree variance reported by OO9. This finding is interesting, given that LRGs in SDSS and those in the BOSS LOWZ sample probe different ranges in color, luminosity, and redshift. Furthermore, the simulations employed to interpret the observations are based on N -body simulations, which differ in their resolution and cosmology, the definition of halo shapes and orientations as well as in the HOD model and the IA model used to produce the mock catalogs that are compared to the observations.

In addition to the constraints on the 2D misalignment, the MICE simulation provides predictions for the distribution of 3D misalignment angles. In Fig. 11, we show the distribution of these misalignment angles, defined as the angle between the 3D major axes \hat{A} before and after randomization for the mock samples of the BOSS LOWZ and the DES surveys. The results for the LOWZ sample

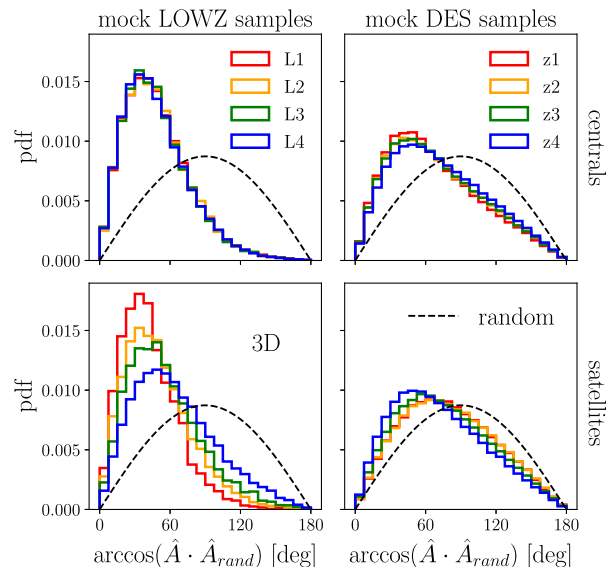


FIG. 11. Distribution of misalignment angles between the 3D major axis A of galaxies in MICE before and after randomization. Results are shown for the different luminosity and redshift subsamples in the mock BOSS LOWZ and DES catalogs, respectively. The black dashed line shows the theoretical expectation for completely randomized orientations.

demonstrate that our IA model implementation for red galaxies works as expected. In our model, the misalignment of red centrals is independent of the galaxy magnitude (Table III), which leads to almost identical distributions of misalignment angles for the different luminosity subsamples. The misalignment angles for satellites are increasing significantly for dimmer samples, as expected from the modeling. Similar trends can be seen for the mock DES samples, although less clearly since these samples consist to $\sim 50\%$ of blue galaxies (Table II), which are almost completely randomized in our model. The distributions of misalignment angles in the DES samples lie therefore closer to a distribution expected for completely randomly oriented objects (shown as dashed line in Fig. 11) than the distributions of misalignment angles in the LOWZ samples.

It is further interesting to note here that the 3D misalignment angles that we obtain from calibrating the IA model in MICE are significantly higher than those found for the galaxy-halo misalignment in the MassiveBlack-II simulation by Tenneti *et al.* [27]. These authors report an average misalignment of ~ 13 degree for galaxies in halos with masses larger than $10^{13} h^{-1} M_\odot$. This prediction is significantly below the values that we find in the MICE LOWZ samples, which reside mostly in halos of that mass range. One potential explanation could be that these authors study the alignment of galaxies with respect to their host subhalo, whereas our results refer to the alignment of galaxies with respect to their host FOF group, which may present a weaker alignment with the central galaxies.

VI. PREDICTIONS FOR TWO-POINT IA STATISTICS

After having validated that MICE is consistent with observational IA constraints from LRGs in SDSS and BOSS, we now proceed by using the simulation to derive predictions at redshift and luminosity ranges that are not covered by these surveys. We are thereby interested in the following three questions. (1) How well do the analytical IA models NLA and TATT fit the IA statistics measured in MICE at the redshifts covered by current photometric weak lensing surveys, such as DES? (2) How do the parameters of these models depend on galaxy color, luminosity, and redshift, and how well do these dependencies agree with observational constraints from surveys other than BOSS, to which the simulation has not been calibrated? (3) How strong is the IA contribution to the observed shear statistics predicted by the simulation in mock DES observations? We address these questions in the following.

A. Dependence of w_{m+} on galaxy magnitude, color, and redshift

In order to test the accuracy of the NLA and TATT models, we fit corresponding predictions for the projected matter-intrinsic shear cross-correlation, w_{m+} (introduced in Sec. II A 1), to the measurements in MICE. Note that using matter instead of galaxies as the density field facilitates the interpretation of our results, as we do not need to take into account inaccuracies of galaxy clustering bias models. However, before discussing these fits, we would like to point out some interesting aspects of the w_{m+} measurements themselves. In Fig. 12, we show these measurements for the 36 volume limited color samples described in Sec. III F. We find that the measurements for samples of blue galaxies are consistent with zero, which confirms that the galaxy-halo misalignment set for these galaxies in the simulation (see Table III) is high enough to eradicate a statistically significant signal at all scales, magnitude, and redshift ranges covered in our analysis. For the red galaxy samples, the measured signal is clearly present, showing dependencies on scale, magnitude, and redshift. At a given redshift, the amplitude of w_{m+} increases with the brightness of the sample. At small scales ($r_p \lesssim 5 h^{-1}$ Mpc), such an increase can be expected from our IA model, since the misalignment of red satellites is set to decrease for brighter magnitudes by the corresponding parameters in Table III. At large scales ($r_p \gtrsim 5 h^{-1}$ Mpc), the w_{m+} alignment signal is dominated by central galaxies (see Fig. 9) for which the galaxy-halo misalignment is set to be independent of the galaxy magnitude. The luminosity dependence of w_{m+} at large scales is hence induced by a change of the host halo alignment. According to the SHAM technique employed for the production of the MICE galaxy catalog, the brightness of central galaxies increases with the mass of their host halos (see Sec. III B). The increase of the alignment of

central galaxies with luminosity is therefore induced by an increase of the host halo alignment with halo mass, which we study in Appendix A [see also [91]].

In addition to the magnitude dependence, we find in Fig. 12 a decrease of the w_{m+} amplitude with redshift for red galaxies within a fixed magnitude range. This redshift dependence is most clearly apparent at large scales. Since our model does not include a redshift dependence of the galaxy-halo misalignment, the decrease of w_{m+} with redshift at large scales is presumably induced by the decrease of the host halo alignment with redshift, which we find in Appendix A. Furthermore, one could expect the w_{m+} signal to decrease, even if halo alignment was redshift independent, due to the decrease of the matter power spectrum amplitude with redshift. We conclude that the interpretation of the luminosity and redshift dependence of IA statistics in terms of galaxy-halo misalignment relies on a detailed understanding of the mass and redshift dependence of halo alignment, which we investigate in Appendix A.

For the comparison between the theory predictions for w_{m+} and the corresponding measurements, which we discuss in the next section, it is interesting to inspect how strongly measurements on different scales are correlated with each other, which is described by the covariance C_{ij} . In Fig. 27, we show examples of the normalized covariance for four of our 36 volume limited samples. We find that the covariances are dominated by the diagonal elements, indicating that the errors on w_{m+} are dominated by noise that originates from the dispersion of intrinsic galaxy ellipticities, which are spatially uncorrelated.

B. NLA and TATT fits to w_{m+} measurement

In order to examine the accuracy of the NLA and TATT models, we fit the corresponding predictions for w_{m+} (Sec. II B 2) to the measurements in MICE (hereafter referred to as the data vector \mathbf{d}) by maximizing the posterior probability $P(\boldsymbol{\theta}|\mathbf{d})$ for the parameter vector $\boldsymbol{\theta}$, given \mathbf{d} , where $\boldsymbol{\theta}$ is given by A_1 and $(A_1, A_2, A_{1\delta})$ in the case of the NLA and the TATT model, respectively. $P(\boldsymbol{\theta}|\mathbf{d})$ is inferred from the likelihood $\mathcal{L}(\mathbf{d}|\boldsymbol{\theta})$ of measuring \mathbf{d} given $\boldsymbol{\theta}$, using Bayes' theorem. We estimate the likelihood from the data, assuming that it is well described by a multivariate normal distribution; i.e.,

$$\ln \mathcal{L}(\mathbf{d}|\boldsymbol{\theta}) = -\frac{1}{2}\chi^2(\mathbf{d}|\boldsymbol{\theta}) + \text{const.} \quad (28)$$

with

$$\chi^2(\mathbf{d}|\boldsymbol{\theta}) = [\mathbf{d} - \mathbf{m}(\boldsymbol{\theta})]^T C^{-1} [\mathbf{d} - \mathbf{m}(\boldsymbol{\theta})]. \quad (29)$$

The model $m(\boldsymbol{\theta})$ is the NLA or TATT prediction for w_{m+} from Eq. (4) for a given $\boldsymbol{\theta}$. The covariance C is estimated from measurements of w_{m+} in jackknife samples as detailed in Sec. II A 1. The posterior is given by Bayes' theorem as

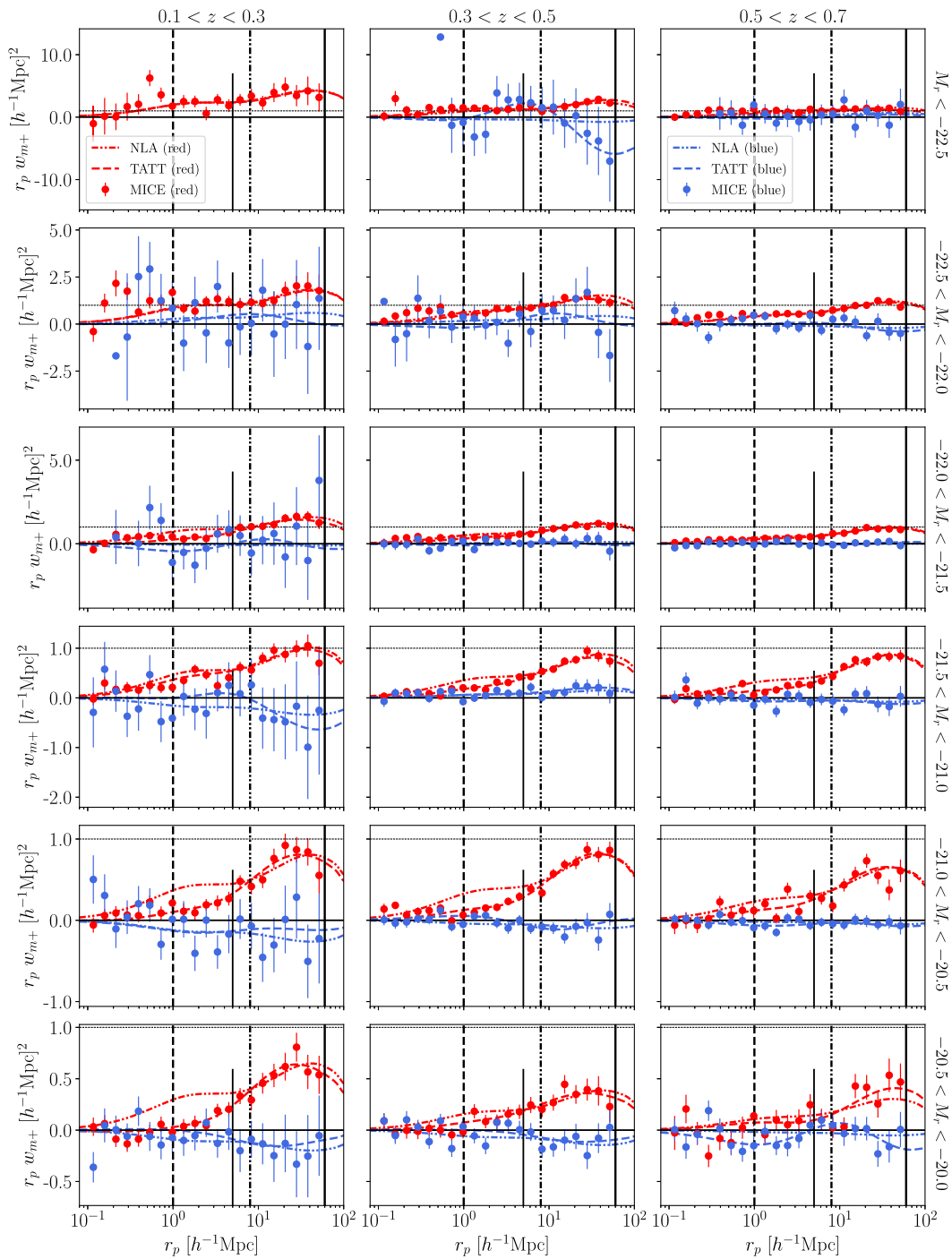


FIG. 12. Projected matter-intrinsic shear two-point correlation functions measured in the 18 volume limited samples shown in Fig. 25. Each sample's range in redshift and absolute r -band magnitude is indicated on the top and right, respectively. Red and blue symbols show measurements in the MICE simulation for red and blue galaxies. Dashed-dotted and dashed lines show fits of the NLA and the TATT model, respectively, where the line color is matched to the corresponding color sample. The lower limits of the fitting ranges are shown for each model as vertical black lines in the corresponding line style. The upper limit is indicated by a vertical black solid line. The dotted horizontal line at $r_p w_{m+} = 1.0$ facilitates the visual comparison of the amplitudes in different samples. Error bars indicate 1σ uncertainties, which can be smaller than the symbol size. The significance of deviations between fits and measurements is shown for various fitting ranges in Fig. 28. Note that results for blue galaxies with $M_r < -22.5$ and $0.1 < z < 0.3$ (top left panel) are not shown because the low number of objects did not allow for meaningful measurements. The absence of the small scale signal in the same magnitude range at higher redshifts results from a lack of bright blue satellites in these samples (see Fig. 25). The short vertical solid lines at $r_p = 5 h^{-1}$ Mpc indicate the scale above which the correlation function is dominated by central galaxies (see Fig. 9).

$$P(\boldsymbol{\theta}|\mathbf{d}) \propto \mathcal{L}(\mathbf{d}|\boldsymbol{\theta})\Pi(\boldsymbol{\theta}). \quad (30)$$

In our analysis, we set the prior $\Pi(\boldsymbol{\theta})$ flat to unity in the interval $[-25, 25]$ and zero elsewhere for all parameters, covering the range of parameter values expected from observations with a high margin. We estimate $P(\boldsymbol{\theta}|\mathbf{d})$ by sampling the parameter space with the Markov-Chain-Monte-Carlo algorithm `emcee` (introduced in Sec. IV A). For each posterior, we run 16 chains with 300 steps each. The best fit parameters are defined as the sampling point with the highest posterior probability. The confidence intervals for each parameter are derived from the corresponding marginalized posterior distribution.

We fit the NLA as well as the TATT model up to scales of $r_p < 60 h^{-1}$ Mpc, which corresponds to the projection length Π , used for the w_{m+} measurements. Blazek *et al.* [92] pointed out that the Limber approximation that enters the w_{m+} prediction requires $r_p \ll \Pi$ to be valid. However, we do not find a significant change in our parameter constraints when reducing the upper limit to $r_p < 30 h^{-1}$ Mpc (see Appendix D), presumably because the likelihood is dominated by small scales measurements, as the measurement errors increase with scale. The lower scale limit of the fitting range is set to 1 and $8 h^{-1}$ Mpc for the TATT and the NLA model, respectively. The choice of these lower limits is motivated in Appendix D. Since we limit the NLA fits to large scales at which satellite galaxy alignment does not affect the w_{m+} amplitude measured in MICE (Fig. 9), we expect the A_1 constrains from the NLA fits to be set solely by the large-scale alignment of central galaxies in the simulation.

We compare the best fits of the NLA and the TATT predictions against w_{m+} measurements in Fig. 12 and find that both models fit the data with similar $\sim 1\sigma$ accuracy at scales above $8 h^{-1}$ Mpc. At smaller scales, the fit of the TATT model stays within the 1σ uncertainties of the data down to the lower limit of the fitting range of $1 h^{-1}$ Mpc. The NLA model tends to lie above the measurements below $8 h^{-1}$ Mpc, which is also the case when reducing the lower limit of the NLA fitting range (see Appendix D). These results indicate that the TATT model provides accurate predictions of galaxy alignment statistics over a wide range of scales, redshifts, and luminosities.

We assess the fitting performance of the IA model predictions for w_{m+} in a more quantitative way in Fig. 13, where we show the minimum χ^2 deviation between measurements and predictions (corresponding to the maximum of the likelihood) per degrees of freedom versus the smallest scale used in the fit. The degrees of freedom are given by $\text{d.o.f.} = n - m$, where n is the number of w_{m+} bins within the fitting range, and m is the number of model parameters ($m = 1, 3$ for NLA, TATT, respectively). The figure confirms the TATT model predictions fit the w_{m+} measurements better than those based on the NLA model as the $\chi^2/\text{d.o.f.}$ values tend to be lower, in particular, at small

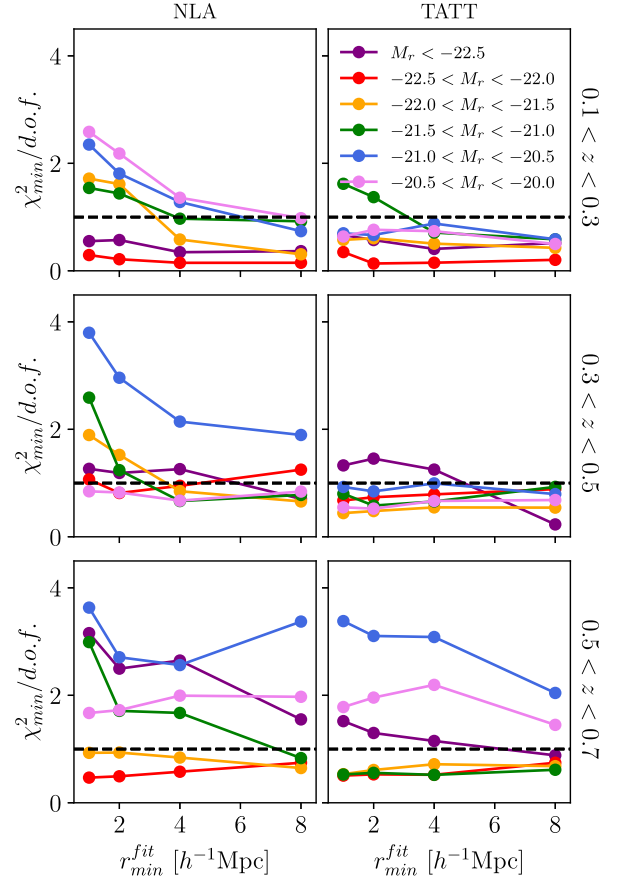


FIG. 13. χ^2 deviation between the best fits of the NLA and TATT model predictions for w_{m+} and the corresponding measurements (as shown in Fig. 12), versus the smallest scale of the fitting range. Results are shown for the 18 volume limited samples of red galaxies in MICE.

scales. We further find the fits to perform better at lower redshifts, which could result from larger errors on the measurements at low redshifts, due to the smaller volume of the light cone (see Fig. 12). Interestingly, we do not find a clear dependence of the fitting performance on the magnitude range probed by the different samples and hence, on the amplitude of w_{m+} . This finding might as well be related to the fact that the different samples have distinct errors, even if they cover the same redshift bin due to their different number densities and noise properties. Inspecting the absolute $\chi^2_{\min}/\text{d.o.f.}$ values shown in Fig. 13, we notice that various results are well below unity. This finding could indicate overfitting of the data by the models. However, the fact that these low values are also present for the NLA model (which has only one free parameter) as well as over a wide range of scales (i.e., different numbers of scale bins m) could be an indication for shortcomings in the χ_{\min} estimation. Such shortcomings may result from the approximations implied in the jackknife method for estimating the covariance, leading, for instance, to an overestimation of the variance. Note that the noise in the

covariance estimates, which we see in the off-diagonal elements in the examples shown in Fig. 27, is expected to reduce the amplitude of the inverse covariance by $\sim 25\%$ for the number of bins and samples used on this analysis [93]. Correcting for this effect of noise would further reduce the χ^2 values by the same factor. When assessing the fitting performance of the IA model predictions, one must further bear in mind that the reference data from MICE is based on a simple model for IA, which provides a good match with the alignment signal of w_{g+} in BOSS LOWZ, but so far, has not been validated against corresponding constraints from other surveys covering different ranges in redshift, luminosity, and color ranges.

C. Dependence of IA model parameters on galaxy magnitude, color, and redshift

We proceed by investigating the dependence of the NLA and TATT model parameters on galaxy redshift, luminosity, and color by comparing the posterior distributions that we derived from the w_{m+} fits in the different volume limited samples from MICE.

We start by inspecting the joint posterior distributions for the TATT parameters (A_1 , A_2 , $A_{1\delta}$), derived from red and blue subsamples at intermediate redshifts and magnitudes ($0.3 < z < 0.5$, $-21.5 < M_r < -21.0$) in Fig. 14. We find the constraints on the parameters for the blue subsample to be consistent with $(A_1, A_2, A_{1\delta}) = (0, 0, 0)$ at the 1σ level. This is expected from the null detection of the w_{m+} (see Fig. 12), which results from the highly randomized orientations of blue galaxies in MICE. Since we find similar results for all blue subsamples, we focus in the following discussion on the parameter constraints from samples of red galaxies. The parameters for the red subsample, shown in Fig. 14, differ significantly from zero, which lines up with the significant signal of the corresponding w_{m+} measurements. We further find the parameter A_2 to correlate weakly with A_1 and slightly stronger with $A_{1\delta}$, while A_1 and $A_{1\delta}$ appear to be uncorrelated. The joint constraints on the TATT parameters from the other volume limited samples (not shown) exhibit a similar behaviour. The dependence of the NLA and TATT parameter constraints on luminosity is shown for the red subsamples in three redshift bins in Fig. 15. In that figure, we display the marginalized posterior distributions as violins at the logarithm of each samples luminosity L , normalized by a pivot luminosity L_0 ; i.e., $\log_{10}(L/L_0) = (\langle M_r \rangle - M_0)/(-2.5)$, where $\langle M_r \rangle$ is each sample's mean SDSS r -band magnitude and $M_0 = -22$, according to literature conventions. We find that the marginalized posteriors of the A_1 parameter in the TATT model are mostly consistent with those from the NLA model, shown as red and blue violins in the top panels of Fig. 15, respectively. However, for certain samples, in particular, in the central redshift bin ($0.3 < z < 0.5$), deviations between the NLA and TATT constraints are significant, while the

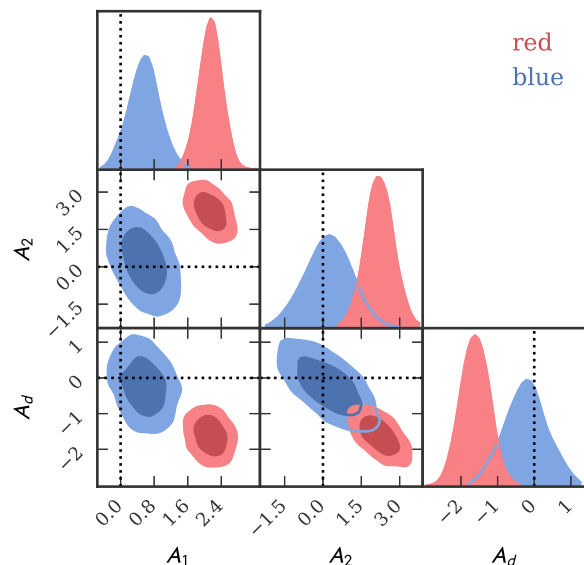


FIG. 14. Posterior probability distribution of the TATT model parameters, derived from fits to the w_{m+} measurements from red and blue galaxies in a volume limited sample, selected by $0.3 < z < 0.5$ and $-21.5 < M_r < -21.0$ (shown in Fig. 12).

general trends of how A_1 changes with redshift and luminosity are the same for both models. These deviations remain significant when varying the scale range over which the TATT model is fitted to w_{g+} (see Fig. 29). We further note that the A_1 constraints are tighter for the NLA than for the TATT model, which can be expected from the higher number of free parameters in TATT.

The A_1 constraints from MICE are compared to observational constraints from various samples of red galaxies from different spectroscopic surveys that were presented in the literature (shown as black symbols in Fig. 15). These observational constraints have been derived analogously to those from MICE from fits of the NLA model to w_{g+} measurements. Circles show results from Joachimi *et al.* [16] for two luminosity samples (L3 and L4) of dim red galaxies in the SDSS-Main sample, two redshift samples of SDSS LRGs (with $z \leq 0.27$), and the MegaZ-LRG sample. Triangles show A_1 constraints from Singh *et al.* [22] for four luminosity subsamples of the BOSS LOWZ sample.¹⁰ Stars show results from Johnston *et al.* [17] for red galaxies in the SDSS main sample and the high and low redshift subsamples from the combined KiDS + GAMA survey. Diamonds show results from Fortuna *et al.* [14] from the KiDS survey for dim and bright subsamples (denoted by the authors as dense and luminous respectively) that cover different ranges of redshifts. Note that the observational results are displayed in Fig. 15 across the three redshift bins

¹⁰These subsamples are similar, although somewhat brighter than the luminosity subsamples from Singh and Mandelbaum [21] to which we calibrate the MICE simulation.

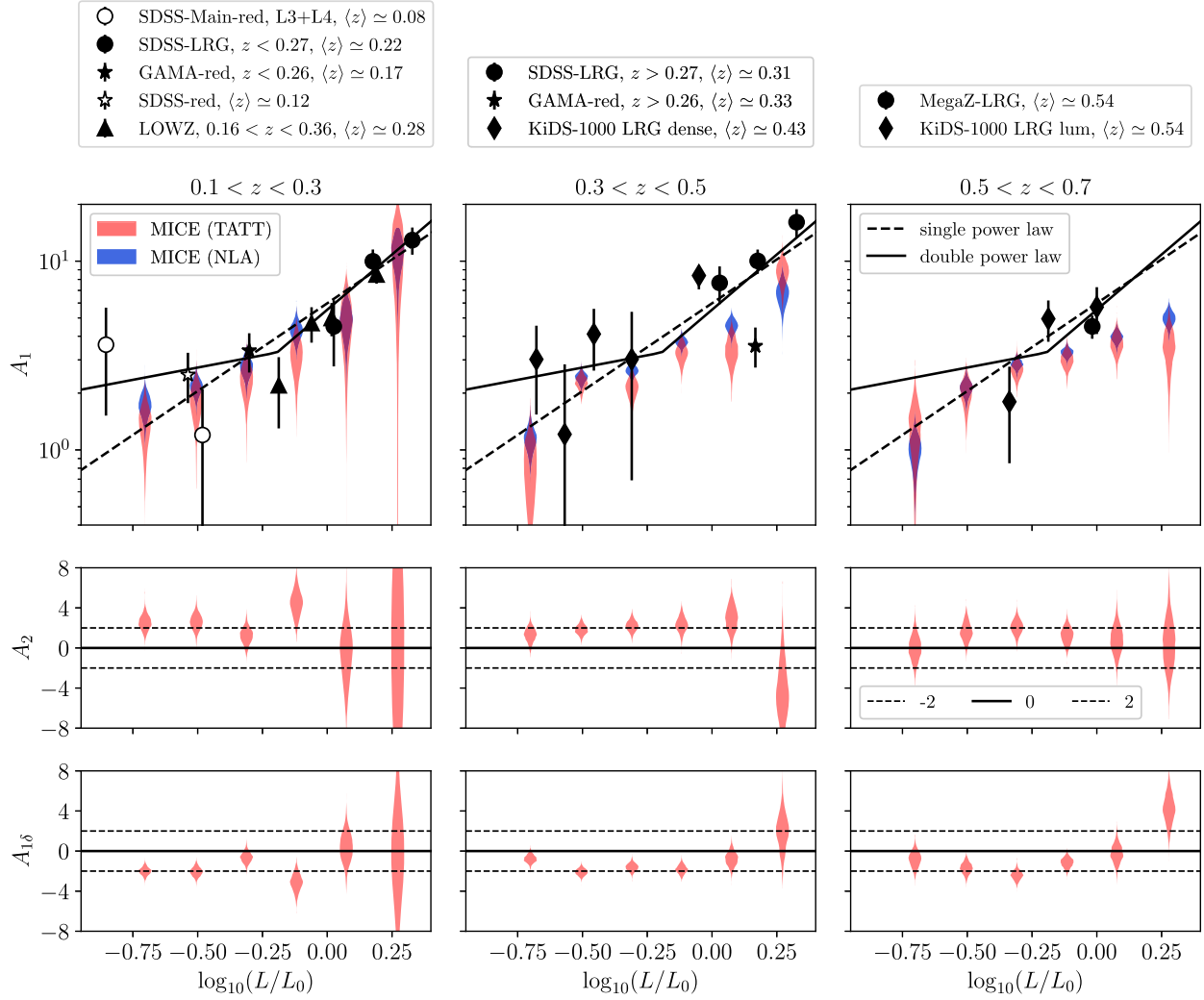


FIG. 15. Marginalized posterior distributions of the NLA and TATT model parameters, derived from fits to w_{m+} measurements for red galaxies in different volume limited samples of the MICE simulation, shown in Fig. 12. The posteriors are displayed at each samples logarithmic mean r -band luminosity, normalized by a pivot luminosity L_0 that corresponds to $M_r = -22$. The top panel shows results for the A_1 parameter, derived from fits of the NLA and the TATT model together with constraints from fits of the NLA model to different w_{g+} measurements in observational samples of red galaxies, provided in the literature (circles: Joachimi *et al.* [16], stars: Johnston *et al.* [17], triangles: Singh *et al.* [22], diamonds: Fortuna *et al.* [14]). Dashed and solid lines show power law fits to the observed data from Fortuna *et al.* [14]. The central and bottom panels show results for the parameters A_2 and $A_{1\delta}$ from the TATT model. The horizontal lines at ± 2 facilitate the comparison of the parameter amplitudes by eye.

in which we analyzed the MICE simulation, according to each samples mean redshift $\langle z \rangle$.

We find in Fig. 15 that most observational constraints on A_1 are consistent with those derived from the volume limited samples in MICE within the estimated errors. This finding is remarkable, given that the MICE IA model has been calibrated only against constraints from LRGs in the BOSS LOWZ sample. Predictions beyond the color-magnitude-redshift range covered by the LOWZ sample rely on the simple assumptions of the IA model. Furthermore, the observational constraints are based on samples of red galaxies from various surveys and have been selected with different cuts on color, magnitude, and redshift. These differences in the selection may

contribute to the deviations between observations and simulation as well as to the variation across the observational constraints. A more meaningful comparison between observations and simulations would require the construction of mock catalogs, which is beyond the scope of this work.

In addition to the observational A_1 constraints from separate surveys, we compare in Fig. 15 the MICE results with two power laws fitted to the combined observational constraints on A_1 , provided by Fortuna *et al.* [14]. We find that the MICE results roughly follow the single power law fit in the lowest redshift bin over the full luminosity range. At higher redshifts, the MICE constraints are still consistent with the same single power law at low luminosities

$(\log_{10}(L/L_0) < -0.25)$ but decrease with redshift for brighter subsamples. This behavior is apparent in the A_1 constraints from the TATT as well as from the NLA model. Since the latter was fitted at $(r_p > 8 h^{-1} \text{ Mpc})$, we attribute the magnitude and redshift dependence of A_1 to be set by the large-scale amplitude of w_{m+} . We argued previously that the large-scale alignment signal is dominated by the alignment of central galaxies (Fig. 9). Given that the misalignment between central galaxies and their host halos is modeled independently of redshift and luminosity, we expect the dependence of A_1 on these quantities to be driven by the redshift and mass dependence of the host halo alignment, which we discuss in Appendix A. Due to a lack of observational constraints on A_1 for luminous, high redshift samples, it remains an open question if the redshift evolution of A_1 for red galaxies as predicted by MICE is supported by observation. However, our results line up with predictions from the Horizon AGN hydrodynamic simulation, according to which, the alignment between massive elliptical galaxies and their surrounding tidal field decreases with redshift [94].

The central and bottom panels of Fig. 15 show the marginalized posteriors for the parameters A_2 and $A_{1\delta}$ of the TATT model. For dim samples ($L < L_0$), we find both parameters to be roughly constant, taking values of $A_2 \sim 2$ and $A_{1\delta} \sim -2$. When approaching brighter luminosities, the parameters switch their sign and reach higher amplitudes for the samples at $z > 0.3$, while constraints at lower redshifts are too noisy to reveal any trend. We further do not find a clear dependence of the A_2 and $A_{1\delta}$ constraints on redshift. Note here that $A_{1\delta}$ in our modeling depends not only on galaxy alignment but also on galaxy clustering, as detailed in Sec. II.

VII. APPLICATION TO DES Y3

After having investigated the IA signal predicted by MICE in volume limited samples, we now study how strongly IA contaminates the lensing signal in the simulated DES-like samples constructed from MICE (see Sec. III E). This predicted contamination was used in the DES Y3 cosmic shear analysis to show that both the NLA and TATT models recover the input cosmology in MICE within the 1σ uncertainties of parameter posteriors. This process provides a valuable test of the modeling since the simulated data is not analytically generated with either model. Note that this investigation becomes possible due to the large area and redshift range covered by the MICE simulation without repetition, while including both the lensing and the IA signal, allowing for separate measurements of the GG, GI, IG, and II terms introduced in Sec. II.

A. Projected matter-intrinsic shear correlation (w_{m+})

In order to compare the IA signal in the DES-like samples with the signal in the volume limited samples,

we measure the w_{m+} statistics, focusing on the lowest two of the four photometric redshift bins, which cover a similar redshift range. The measurements are shown in Fig. 16 for the full sample in each bin as well as for the red and blue subsamples, which are defined by our $u - r = 0.94$ color cut, as shown in Fig. 23. We find the strongest signal for the red subsample and no significant signal for the blue subsample, while the signal for the full sample lies between those of the two subsamples. The color dependence is expected from our modeling as well as from the w_{m+} measurements in the volume limited samples. The amplitudes of the full samples and the red subsamples are comparable to those derived from red galaxies in our dimmest volume limited samples (Fig. 12), showing that the IA contamination in our DES-like samples is relatively weak. This finding is consistent with the large galaxy-halo misalignment angles for the DES-like samples, shown in Fig. 11.

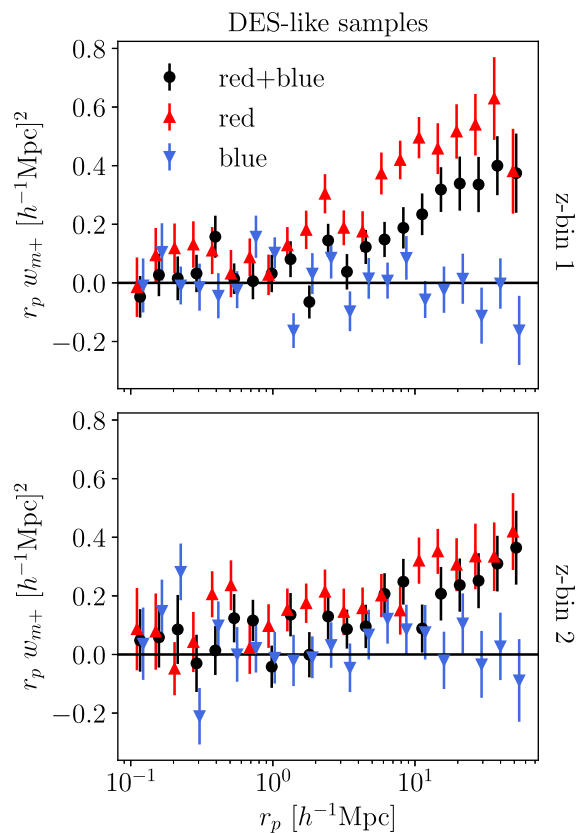


FIG. 16. Projected matter-intrinsic shear correlation, measured in the two lowest redshift bins of the DES-like sample constructed from MICE. Results are shown for the full sample as well as for subsamples of red and blue galaxies. The amplitudes are comparable to those from our measurements in the dimmest volume limited samples (i.e., $r_p w_{m+} \lesssim 0.5 h^{-2} \text{ Mpc}^2$; see Fig. 12), showing that the IA contamination in the DES-like samples is predicted to be weak. Symbols for the red and blue subsamples are slightly shifted along the r_p -axis for clarity.

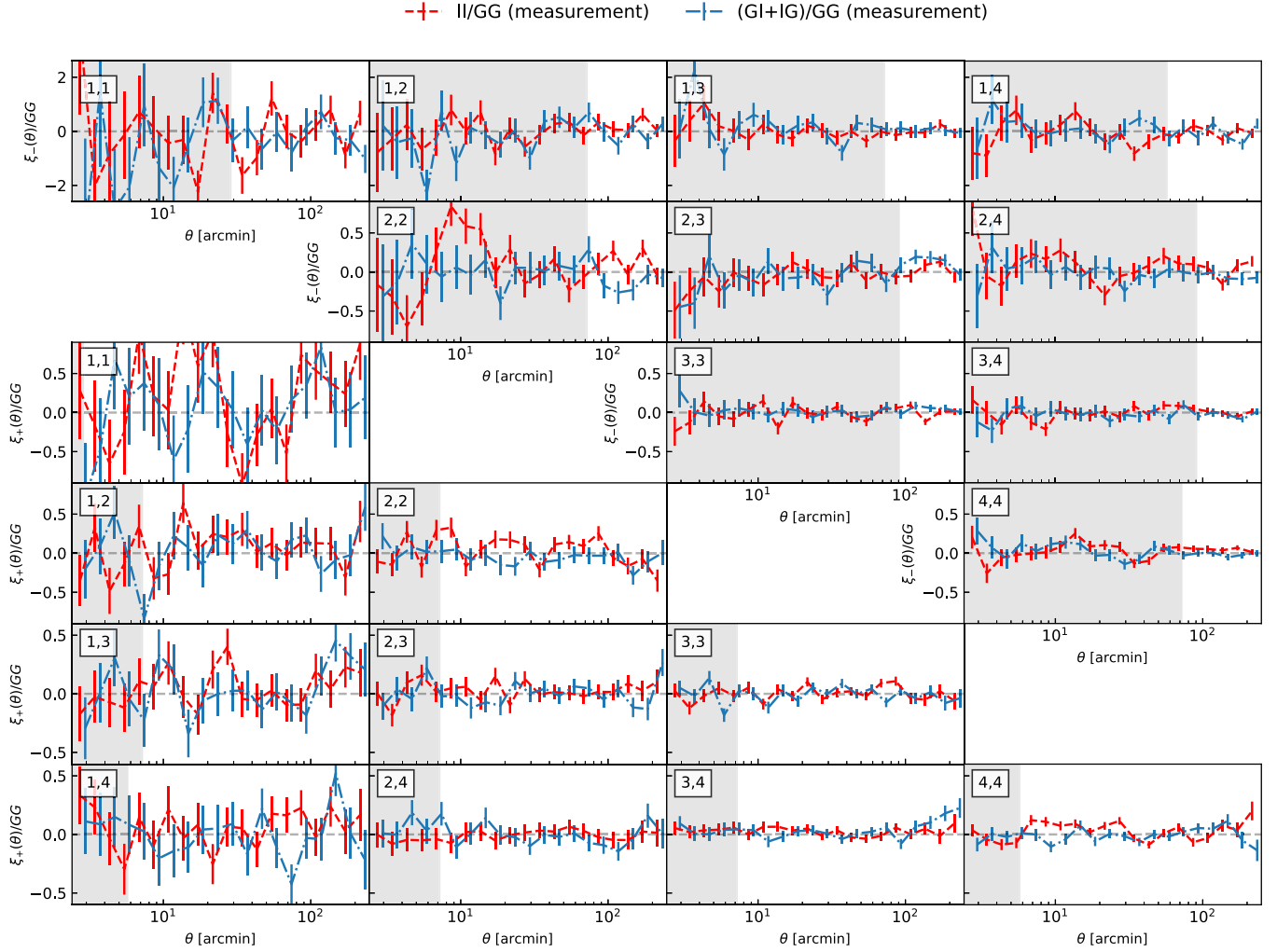


FIG. 17. Intrinsic alignment correlation functions as measured from combinations of the individual G and I ellipticities in MICE, divided by the theory GG signal computed at the MICE cosmology and with the mock redshift distributions. Different panels show cross-correlations of redshift bins in ξ_+ and ξ_- , and shaded bands correspond to the scales that are removed from the inference of cosmological and nuisance parameters. Error bars indicate the estimated 1σ shape noise uncertainties.

B. Angular shear-shear correlation (ξ_{\pm})

We focus now on the angular shear-shear correlation ξ_{\pm} , which was introduced in Sec. II and used in the cosmological weak lensing analysis of the DES Y3 data release. In Fig. 17, we show the ξ_{\pm} measurements of the IA terms that contribute to the cosmic shear signal, $GI + IG$ and II , divided by the theoretical GG signal computed at the cosmology and redshift distributions of the MICE mock. Each panel corresponds to a different cross-correlation between redshift bins, and the shaded bands correspond to angular scales that are removed from the cosmic shear cosmology inference, mainly due to the effect of baryonic feedback (see [95], Secco and Samuroff *et al.*, [48] for a justification).

We find that the amplitudes of the IA signals compared to GG is small and consistent overall with shape noise fluctuations. This finding indicates that the alignment signal, which we found to be weak but significantly above

the noise level in the w_{m+} measurements for the DES-like samples in Fig. 16, falls below the noise level when probing it in the same samples with angular statistics. We attribute this decrease in signal-to-noise to the projection over large line-of-sight distances that is implied in the definition of angular correlations.

C. Results of likelihood analysis

In order to produce a likelihood analysis with the measured data vector, we construct an analytic Gaussian covariance using `COSMOCOV`¹¹ [96] for the present DES-like MICE sample, matching the statistical power of DES Y3 [see the description in Appendix A of [48]]. The theory prediction in the likelihood evaluation is summarized in Eq. (13) [with $C(\ell)$ spectra containing IA

¹¹<https://github.com/CosmoLike/CosmoCov>.

contributions], and we ultimately infer the posteriors on cosmological and nuisance parameters of the $\xi_{\pm}(\theta)$ model.

For this inference, we sample the parameter space utilizing POLYCHORD [97], with similar performance settings as those used in the DES Y3 analyses. Our flat Λ CDM cosmology model has six free parameters: the matter density Ω_m , the baryon density Ω_b , the primordial amplitude A_s , the spectral index n_s , the Hubble parameter h , and the neutrino density $\Omega_\nu h^2$. We additionally vary eight calibration parameters (a shear multiplicative bias m_i and a photo- z shift parameter Δz_i for each redshift bin i). Freeing these nuisance parameters is not strictly required in our present analysis, which does not include shear and photo- z systematics but are important to guarantee a roughly similar figure of merit between this exercise and the actual DES Y3 analysis. In addition, we also vary two IA parameters in the NLA model (A_1 and its redshift evolution power-law η_1) and five parameters for the TATT model (both NLA parameters plus a galaxy bias parameter b_{TA} and the amplitude and redshift evolution of torquing terms, A_2 and η_2). We note that this choice follows closely the DES Y3 analysis: We explicitly parametrize the impact of the linear bias of the source galaxies contributing to the tidal signal as $A_{1\delta} = b_{TA}A_1$, allowing for extra freedom in the model. This fiducial setting thus includes 19 (22) free parameters. The explicit priors on these cosmological and nuisance parameters are generally uninformative and can be found in, e.g., Secco and Samuroff *et al.*, [48], Table I.

In addition to this fiducial setting, we also run inferences with cosmological parameters fixed at the known MICE truth values and shear and redshift calibration parameters fixed at zero (thus freeing only the IA model parameters) and a “baseline” analysis in which no IA signals are added, in which case, we expect IA constraints to be compatible with zero. In the baseline scenario, we find IA posteriors to be consistent with zero, in line with our expectations:

$$A_1 = -0.32_{-0.25}^{+0.57} \quad (\text{TATT baseline}),$$

$$A_2 = -0.10_{-0.59}^{+0.74} \quad (\text{TATT baseline}),$$

where the central values are the maxima of the marginalized posterior distributions and the upper and lower values are the distances to the bounds of the corresponding 68% confidence intervals.

The main IA constraints as probed by ξ_{\pm} with this DES-like source sample come from the simplified, fixed-cosmology scenario. In this reduced parameter space, we find, when fitting NLA:

$$A_1 = -0.11_{-0.27}^{+0.21} \quad (\text{NLA with fixed cosmology}),$$

and similarly we find, for the TATT model:

$$A_1 = -0.30_{-0.51}^{+0.49} \quad (\text{TATT with fixed cosmology}),$$

$$A_2 = 0.67_{-0.41}^{+1.23} \quad (\text{TATT with fixed cosmology}).$$

In all of the cases above, we find A_1 parameters that are consistent with zero within one standard deviation and only find a marginal preference for positive A_2 in the case of TATT at a fixed cosmology. These results are not unexpected given the overall small impact on the DES-like source sample as a fraction of the GG signal, as seen in the correlation functions shown in Fig. 17.

Finally, for the cases where we additionally vary cosmological and nuisance parameters, when fitting the data vector with the NLA model, we find:

$$A_1 = -0.51_{-0.27}^{+0.62} \quad (\text{NLA with free cosmology \& nuis.}),$$

and similarly when employing the TATT model:

$$A_1 = -0.55_{-0.33}^{+0.71} \quad (\text{TATT with free cosmology \& nuis.}),$$

$$A_2 = -0.37_{-1.65}^{+1.68} \quad (\text{TATT with free cosmology \& nuis.}).$$

These results are also in line with our expectations based on Fig. 17: The overall IA amplitudes are consistent with zero within a standard deviation, and the constraining power on the individual 1D parameters is suppressed with respect to the fixed cosmology analogs since there is a greater number of parameters in the likelihood analysis, weakening those constraints. Apart from IA, the cosmological parameters of main importance for this type of analysis are the amplitude S_8 and the matter density Ω_m , which are presented for this simulated MICE sample in Secco and Samuroff *et al.*, [[48] Appendix A] and found to be unbiased with respect to the MICE input cosmology.

In conclusion, utilizing a cosmic shear measurement obtained from the DES-like simulated source sample, we find that IA amplitudes are subdominant as a contributor to the tomographic $\xi_{\pm}(\theta)$ data vector and that, accordingly, posterior distributions on IA parameters for both TATT and NLA models are largely consistent with zero. In tandem, the analysis presented in [48] also shows, using the same simulated mock catalog, that inferring cosmological parameters with both IA models recovers the input MICE simulation cosmology without biases.

We emphasize that these results are specific to our simulation, which was calibrated to match the IA signal of LRGs at relatively low redshifts, while assuming effectively no alignment for blue galaxies, which constitute a significant fraction of the DES-like samples (see Sec. III E).

VIII. SUMMARY AND CONCLUSIONS

We implemented intrinsic galaxy alignment (IA) in the light-cone output of the cosmological simulation MICE to study it as a contamination in measurements of two-point correlation functions from weak lensing observations of the cosmic large-scale structure. The simulation was thereby used for two purposes: (a) to investigate the accuracy of analytical models that describe the IA contamination at

luminosities and redshifts for which observational constraints from spectroscopic surveys are currently not available and (b) to predict the IA contamination in the weak lensing observations of the Dark Energy Survey (DES). We thereby take advantage of the fact that MICE provides both, the intrinsic as well as the gravitational shear components. For the IA implementation, we use a semi-analytic model to assign a shape and an orientation to each galaxy of the HOD-SHAM catalog of the MICE simulation, taking into account the galaxy's brightness and color as well as the orientation and angular momentum of its host halo. Our model is inspired by semianalytic IA models presented previously in the literature [e.g., [36,37]] but includes substantial advancements in three aspects.

1. We developed a new method for assigning 3D galaxy shapes, assuming a simple ellipsoidal morphology for each object. The parameters of this shape model were calibrated such that the distribution of projected 2D axis ratios matches observational constraints from the COSMOS survey for different ranges of galaxy color, absolute magnitude, and redshift (Sec. IV).
2. The misalignment between the orientations of galaxies and those of their host halos was calibrated such that the projected galaxy-intrinsic shear correlation (w_{g+}), measured in a mock BOSS LOWZ sample of LRGs from MICE, matches direct IA measurements in the corresponding observations from Singh and Mandelbaum [21] in four different magnitude bins over a large range of scales ($0.1 < r_p < 200 h^{-1}$ Mpc; see Sec. V). We found that the galaxy-halo misalignment for LRGs in MICE is consistent with constraints derived by Okumura *et al.* [35].
3. The MICE light cone covers one octant of the sky ($\sim 5000 \text{ deg}^2$) and reaches up to redshift $z = 1.4$. The simulated IA catalog is therefore the largest presented in the literature so far, which allows us to construct realistic mock catalogs of current weak lensing surveys and measure the IA signal with high significance.

In our investigation of the accuracy of analytical IA models, we focus on the NLA model and the TATT model. We assess the models' accuracy by comparing their predictions for the projected matter-intrinsic shear correlation (w_{m+}) against corresponding measurements in MICE (Sec. VI). The latter are derived for a set of volume limited samples of red and blue galaxies that span over the redshift range $0.1 < z < 0.7$ and probe absolute magnitudes down to $M_r = -20$. In contrast to observations, the simulation allows us to access the matter field directly, which significantly reduces the impact of galaxy bias on the IA statistics. As discussed in Sec. II, we can therefore study the accuracy of IA modeling with less sensitivity to the details of nonlinear galaxy bias than when using the observable w_{g+} .

Our w_{m+} measurements in MICE show strong dependencies on galaxy color, magnitude, and redshift, which allow one to test the analytical models in a wide range of possible alignment scenarios (Fig. 12). We find that the NLA and the TATT model fit the w_{m+} measurements with similar accuracy when restricting the fit to scales larger than $8h^{-1}$ Mpc as deviations from the measurements are consistent with the $\sim 1\sigma$ error estimates. When including smaller scales, the NLA model breaks down, while the TATT model retains a $\sim 2\sigma$ accuracy down to the smallest scale considered of $1h^{-1}$ Mpc (Fig. 28). It is important to keep here in mind that the IA signal predicted in MICE is based on assumptions employed in the HOD and semi-analytic IA modeling, which might be too simplistic. However, the fact that the w_{g+} signal in MICE matches the BOSS observations, even in the one-halo regime below $1h^{-1}$ Mpc, is an indication that these simplistic assumptions provide reasonably effective descriptions of the true galaxy alignment.

As an additional validation of the simulation, we compare the constraints on the NLA and TATT parameter A_1 , which is sensitive to the IA signal at large scales, to constraints from the literature that were derived from various observed samples of red galaxies to which the MICE simulation has not been calibrated (Fig. 15). We find that the A_1 constraints from MICE are in broad agreement with the observations, given the large error bars and taking into account that the selection of the volume limited samples in MICE differs significantly from the selection of the observed samples. At low redshifts ($z \leq 0.3$), the luminosity dependence of the A_1 parameters in MICE is consistent with a single power law, which was derived from fits to observational A_1 constraints for red galaxies by [14], while the broken power law proposed by these authors shows clear deviations from our results. At higher redshifts ($z > 0.3$), the luminosity dependence of A_1 for red galaxies in MICE decreases, which is mainly driven by a decrease of the alignment amplitude for LRGs. As for low redshifts, this luminosity dependence seems to be better described by a single, rather than a broken power law. Verifying the high redshift predictions from MICE will be possible with IA measurements in upcoming spectroscopic surveys, such as DESI or PAU.

The alignment parameters for samples of blue galaxies in the simulation are consistent with zero (Fig. 14). This result is expected since central blue galaxies are oriented in our model with the host halos' angular momentum, for which we find only a weak alignment signal in Appendix A. Furthermore, we highly randomize the orientations of these objects to ensure that the simulation reproduces the null detection of IA for blue galaxies in current observations.

As a last step in our analysis, we investigate the contribution of IA to the angular shear correlation ξ_{\pm} in mock samples of the DES survey, taking advantage of the fact that the simulation allows us to measure the GG, II, and

GI term separately from each other. Interestingly, the II and the GI terms predicted for the DES samples by MICE are consistent with zero (Fig. 17). We have validated that the w_{m+} measurements for the same samples show a signal that is significant with respect to the errors. However, the amplitude of this signal is relatively low compared to our measurements for red galaxies, which can be expected from the $\sim 50\%$ fraction of blue galaxies that the simulation predicts for the DES-like samples (Table II). A possible reason for the nondetection of the II and GI terms in MICE could be that the angular shear statistics ξ_{\pm} is less sensitive to IA contaminations than the projected statistics w_{m+} , as it probes the integrated IA signal over a wide range of redshifts, including galaxy pairs with large physical separations that are only weakly intrinsically aligned. The resulting decrease in the signal-to-noise ratio could lead to a null detection for the IA terms in the angular statistics.

A weak IA signal in angular statistics lines up with findings of Wei *et al.* [39], who study IA contaminations in mock observations of the weak lensing surveys KiDS and DLS using a semianalytic model to implement IA in the Elucid simulation. In contrast to our results, these authors find a weak but still significant IA contribution to the GG signal. One potential reason for that difference may be the use of constraints on galaxy-halo misalignment angles that were derived from LRGs for the entire KiDS sample in that work. This could result in an overly high signal, as LRGs show the strongest alignment signal compared to other galaxy populations (see, e.g., Fig. 15).

Another reason for the weak alignment in the DES-like samples could be the fact that predictions for the alignment of dim galaxies (which constitute a significant part of the sample) are presumably affected by the relatively low mass resolution, causing noise in the measured host halo orientations and hence decreasing the predicted galaxy alignment (see Appendix A). However, a weak contribution of IA in DES-like samples lines up with recent findings from Secco and Samuroff *et al.*, [48], who derive constraints on IA model parameters from the cosmological analysis of the cosmological weak lensing signal and find those to be consistent with zero.

We stress here that the IA predictions from the MICE simulation for DES-like samples need to be taken with caution since the simulation has only been tested directly against IA observations from red galaxies at redshift that are well below those probed by DES. Furthermore, the DES samples contain a high fraction of blue galaxies, in particular, at high redshifts (Table II), for which the simulation predicts no IA signal by construction. This lack of alignment has been observed for blue galaxies at low redshifts. However, the alignment of blue galaxies at high redshifts remains unconstrained by observations.

Future improvements of the simulation could therefore consist in taking into account IA observations at higher redshifts from upcoming spectroscopic surveys. An

interesting extension of our work in that regard based on current observations would be to reduce the misalignment of blue galaxies, such that the simulation reproduces the observed null detection for this type of galaxies (e.g., from direct measurements in a SDSS sample [17] or indirect measurements in DES Y1 data [88]) within the corresponding errors. Such a decrease of misalignment may lead to more significant IA contributions to the predicted DES Y3 lensing signal.

An additional improvement of our modeling could consist in a more realistic selection of discs and ellipticals, for instance using two different color indices as discussed in Sec. III C. In our current implementation all galaxies defined as red by a single color index cut are treated as ellipticals and are therefore aligned with their host halos principle axes. A more sophisticated color cut could identify a fraction of red objects as discs and align them with their host halo's angular momentum vector, which might change the predictions of our simulation. One shortcoming which is harder to address is that a significant fraction of galaxies have an irregular morphology, which is currently not taken into account in the modeling. Hydrodynamic simulations may help to find an effective model that describes the intrinsic alignment of such galaxies. More realism could further be added to the simulation by introducing a dependence of satellite alignment on the distance to the host halo center, which has been found in observations [98,99] as well as in hydrodynamic simulations [100].

There are several potential applications of our IA simulation not explored here, for instance, studies of IA in third-order lensing correlations [101,102], in particular, because such statistics have been detected at high signal-to-noise in recent DES Y3 data [103]. Another application would be to study priors on the IA modeling, in particular, on TATT parameters that are poorly constrained otherwise.

We expect that the unique size and depth of the MICE IA simulation presented here and the improvements in the IA assignment model will play a central role in constraining our understanding of the IA contribution in ongoing and future weak lensing observations.

IX. DATA AVAILABILITY

The MICE IA simulation presented in this work as well as the halo catalog used in the modeling are publicly available at CosmoHub¹² [104,105]. A public version of our IA simulation code is available on GitHub.¹³

ACKNOWLEDGMENTS

We thank Christopher Bonnett for the initial idea to implement IA in MICE. We thank Sukhdeep Singh and

¹²<https://cosmohub.pic.es>.

¹³<https://github.com/kaidhoffmann/genIAL>.

Rachel Mandelbaum for providing w_{g+} measurements from the BOSS LOWZ sample. We thank David Navarro for useful comments on the draft. K. H. acknowledges support by the Swiss National Science Foundation (Grant Nos. 173716, 198674), and from the Forschungskredit Grant of the University of Zurich (Project No. K-76106-01-01). J. B. and S. S. are partially supported by NSF Grant AST-2206563. This work was also partly supported by the program “Unidad de Excelencia María de Maeztu CEX2020-001058-M.” CosmoHub is hosted by the Port d’Informació Científica (PIC), maintained through a collaboration of Centro de Investigaciones Energéticas, Medioambientales y Tecnológicas (CIEMAT) and Institut de Física d’Altes Energies (IFAE), with additional support from Universitat Autònoma de Barcelona (UAB). Funding for the DES Projects has been provided by the U.S. Department of Energy, the U.S. National Science Foundation, the Ministry of Science and Education of Spain, the Science and Technology Facilities Council of the United Kingdom, the Higher Education Funding Council for England, the National Center for Supercomputing Applications at the University of Illinois at Urbana-Champaign, the Kavli Institute of Cosmological Physics at the University of Chicago, the Center for Cosmology and Astro-Particle Physics at the Ohio State University, the Mitchell Institute for Fundamental Physics and Astronomy at Texas A&M University, Financiadora de Estudos e Projetos, Fundação Carlos Chagas Filho de Amparo à Pesquisa do Estado do Rio de Janeiro, Conselho Nacional de Desenvolvimento Científico e Tecnológico and the Ministério da Ciência, Tecnologia e Inovação, the Deutsche Forschungsgemeinschaft and the Collaborating Institutions in the Dark Energy Survey. The Collaborating Institutions are Argonne National Laboratory, the University of California at Santa Cruz, the University of Cambridge, Centro de Investigaciones Energéticas, Medioambientales y Tecnológicas-Madrid, the University of Chicago, University College London, the DES-Brazil Consortium, the University of Edinburgh, the Eidgenössische Technische Hochschule (ETH) Zürich, Fermi National Accelerator Laboratory, the University of Illinois at Urbana-Champaign, the Institut de Ciències de l’Espai (IEEC/CSIC), the Institut de Física d’Altes Energies, Lawrence Berkeley National Laboratory, the Ludwig-Maximilians Universität München and the associated Excellence Cluster Universe, the University of Michigan, NSF’s NOIRLab, the University of Nottingham, The Ohio State University, the University of Pennsylvania, the University of Portsmouth, SLAC National Accelerator Laboratory, Stanford University, the University of Sussex, Texas A&M University, and the OzDES Membership Consortium. Based in part on observations at Cerro Tololo Inter-American Observatory at NSF’s NOIRLab (NOIRLab Prop. ID 2012B-0001; PI: J. Frieman), which is managed by the Association of

Universities for Research in Astronomy (AURA) under a cooperative agreement with the National Science Foundation. The DES data management system is supported by the National Science Foundation under Grant Nos. AST-1138766 and AST-1536171. The DES participants from Spanish institutions are partially supported by MICINN under Grant Nos. ESP2017-89838, PGC2018-094773, PGC2018-102021, SEV-2016-0588, SEV-2016-0597, and MDM-2015-0509, some of which include ERDF funds from the European Union. IFAE is partially funded by the CERCA program of the Generalitat de Catalunya. Research leading to these results has received funding from the European Research Council under the European Union’s Seventh Framework Program (FP7/2007-2013) including ERC Grant Nos. 240672, 291329, and 306478. We acknowledge support from the Brazilian Instituto Nacional de Ciência e Tecnologia (INCT) do e-Universo (CNPq Grant 465376/2014-2). This manuscript has been authored by Fermi Research Alliance, LLC under Contract No. DE-AC02-07CH11359 with the U.S. Department of Energy, Office of Science, Office of High Energy Physics.

APPENDIX A: DARK MATTER HALO ALIGNMENT

1. Effects of noise in halo orientations

We investigate here the impact of noise resulting from low halo particle numbers on halo alignment statistics in MICE. For that purpose, we select halos in the MICE light cone with $N_p \gtrsim 320$ particles ($M_h \gtrsim 10^{12.97} h^{-1} M_\odot$), then select randomly a subset of N_{rand} particles from these halos without replacement and measure the halo major axis and angular momentum vectors (\mathbf{A} and \mathbf{J} , respectively) as detailed in Sec. III B 1. Finally, we measure the 3D alignment statistics of these halos with the large-scale structure as

$$\eta_X(r) = \langle |\hat{\mathbf{X}}_1 \cdot \hat{\mathbf{r}}| \rangle(r) - 1/2, \quad (\text{A1})$$

which is the inner product of the unit vectors $\hat{\mathbf{X}}$ and $\hat{\mathbf{r}}$, where \mathbf{X} refers to either \mathbf{A} or \mathbf{J} , \mathbf{r} is a vector pointing to a neighboring halo, and $\langle \dots \rangle$ denotes the average over all halo pairs separated by the distance r . Relative orientations of \mathbf{X} and \mathbf{r} that are random, parallel, and perpendicular to each other lead to $\eta_X = 0$, > 0 , and < 0 , respectively. In Fig. 18, we compare our measurements of η_A and η_J for various values of N_{rand} . We find a positive amplitude of η_A , which indicates that the major axes tend to point toward neighboring halos. The amplitude starts to decrease significantly for $N_{\text{rand}} \lesssim 80$. At $N_{\text{rand}} = 10$, the amplitude is decreased by roughly 30%, while we still find a clear signal.

The amplitude of η_J is mostly negative, indicating that the halos’ angular momenta tend to be aligned perpendicular to the vector pointing toward neighboring halos. We see no clear dependence of η_J on N_{rand} , as we saw it for η_A . A potential explanation for that finding could

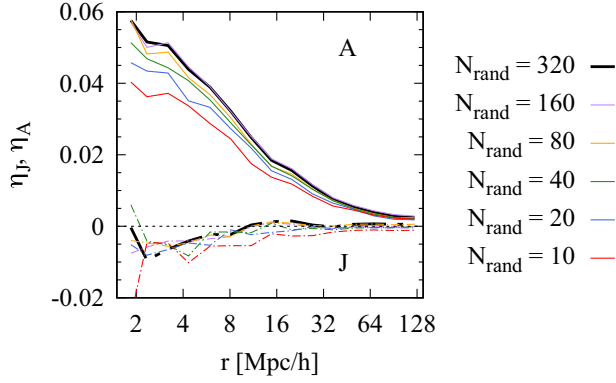


FIG. 18. 3D halo alignment statistics quantifying the average alignment of the major axis and angular momentum of dark matter halos in MICE (**A** and **J**, solid and dashed lines, respectively) and the vector \mathbf{r} pointing to neighboring halos, as defined in Eq. (A1). Results are shown for halos at $z = 0.25$ with more than $N_p = 320$ particles ($M_h \gtrsim 10^{12.97} h^{-1} M_\odot$). N_{rand} indicates the number of random particles per halo from which **A** and **J** were measured. $\eta = 0$ corresponds to random alignment.

be that the dispersion of the particles' angular momentum directions is low for the halos used in our test, such that the average does not vary much across different random subsets of particles. Another interesting result is that the absolute values of η_J are significantly lower than those of η_A . The lower amplitude of η_J implies that blue galaxies, which are aligned with **J** in our simulation, will always show a significantly weaker IA signal than red galaxies, which are aligned with **A**, unless we set a much stronger misalignment for red than for blue galaxies.

2. Mass and redshifts dependence

We consolidate this last point by comparing the amplitudes of η_J with those of η_A as well as η_C for halos in four mass samples at three different redshifts of the MICE light cone in Fig. 19. For η_A , we find positive amplitudes for all mass and redshift samples. The amplitudes are increasing with the halo mass and decrease with redshift. Overall, the redshift dependence is relatively weak compared to the mass dependence, in particular, for low halo masses. This finding explains why the large scale amplitudes of w_{g+} in Fig. 10 and the corresponding A_1 parameter in Fig. 15 are decreasing more strongly with redshift for luminous than for dim samples since the luminous galaxies reside in more massive halos than dim galaxies. The fact that η_A increases more strongly with halo mass than with redshifts may be partially explained by the mass-dependent noise on the halo orientations, causing a weaker alignment for lower halo masses. However, the resolution effects on η_A that we show in Fig. 18 are weaker than the mass dependence in Fig. 19. The results for η_C are similar to those η_A , while the amplitudes are negative since $\mathbf{C} \perp \mathbf{A}$.

The results for η_J line up with the results from Fig. 18 as the amplitude is weaker than for η_A and η_C for all redshift

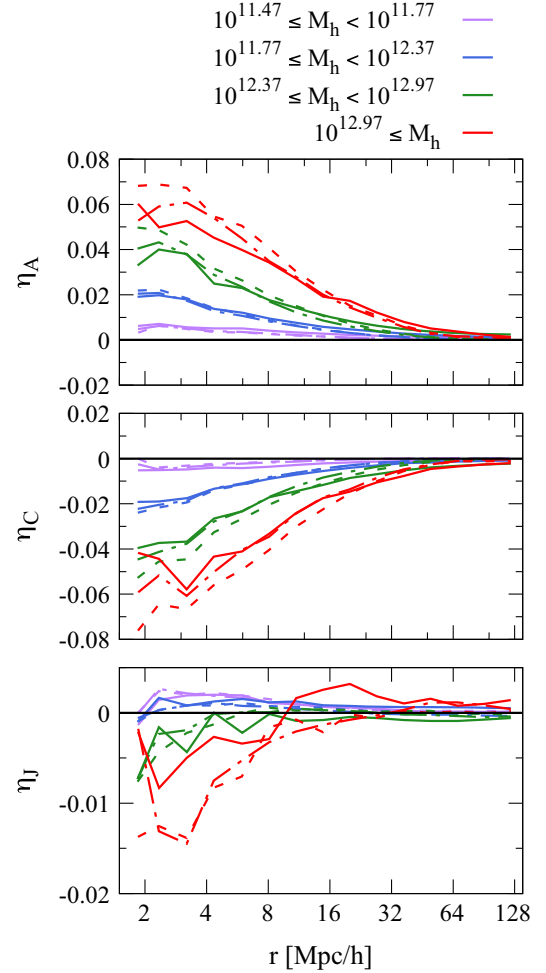


FIG. 19. 3D halo alignment statistics of the halo major axis, minor axis, and angular momentum in the MICE simulation (top, central, and bottom panels, respectively). Results are shown for halos in the four mass ranges that are indicated on the top. The limits at $\log_{10}(M_h) = (11.47, 11.77, 12.37, 12.97)[\log_{10}([h^{-1} M_\odot])]$ correspond to $N_p = (10, 20, 80, 320)$ particles per halo. Solid, dashed-dotted, and dashed lines show results at the redshifts $z = 0.2, 0.7$ and 1.2 , respectively.

and mass samples. A similar finding has been reported by Forero-Romero *et al.* [106], who compare the alignment amplitude of halo shapes and angular momenta with the large-scale structure in a cosmological simulation. This consolidates our expectation that blue galaxies in our simulation would be weakly aligned compared to red galaxies, even when setting a lower misalignment for blue galaxies than used in our current model. It is further interesting to note that η_J shows a more complex dependence on mass and scale than η_A and η_C . For massive objects, we find the amplitude to switch from negative to positive for increasing scales, indicating a change in the orientations of **J** from perpendicular to parallel with respect to neighboring halo directions. Another sign flip occurs at small scales ($r \lesssim 20 h^{-1}$ Mpc) between low and high mass samples. Such a flip has also been found in other simulation-based

studies of halo spin alignment [e.g., [106–108]]. However, a detailed discussion of these findings is beyond the scope of this work.

APPENDIX B: COLOR, MAGNITUDE, AND REDSHIFT DISTRIBUTIONS

1. BOSS LOWZ

In Fig. 20, we compare the distribution of m_r , c_{\parallel} , and c_{\perp} [defined in Eq. (21)] of galaxies in MICE to observations from the BOSS LOWZ Data Release 11¹⁴ in the combined Southern and Northern Galactic Pole, focusing on the SM16 redshift range. We find a reasonable agreement between the observed and simulated distributions. However, when applying the LOWZ cuts on MICE with $\Delta m_r = 0$, we find a $\sim 16\%$ lower number density than in the observations. The latter is obtained from the number of LOWZ Data Release 12 galaxies in the SM16 redshift range, $N_g = 249938$, and the corresponding effective area of $A = 8,579 \text{ deg}^2$, given in Table II of Reid *et al.* [109], which leads to $n_g = N_g/A_{\text{eff}} = 29.97$. We therefore adjust the cuts on m_r in MICE $\Delta m_r = 0.085$, which results in a $\sim 0.2\%$ agreement in the observed number density, with 154617 galaxies in the 5156.62 deg^2 octant of the MICE simulation.

Note that the LOWZ catalog used by SM16 is slightly reduced in size and density compared to the original LOWZ sample since only galaxies for which three different shape measurements were available were used in that analysis. As a result, dim objects were excluded from their analysis, and the average brightness is increased to some degree. One can therefore expect the clustering amplitude in the LOWZ sample to be slightly increased. Including the exact same selection effects in the mock construction is not feasible as the MICE simulation does not include the relevant observational systematics. However, we do not expect these effects to be critical, since the clustering amplitude in our mock is in good agreement with the observations (Fig. 3).

The selection of luminosity subsamples in the mock BOSS LOWZ sample from MICE is illustrated in the top panel of Fig. 21, where we show the joint magnitude-redshift distribution. The bottom panel of the same figure compares the redshift distribution of the subsamples in MICE LOWZ with the observed redshift distribution from the BOSS DR11. We find that the redshift distribution of the MICE subsamples L1-L3 are consistent with the observations, while the dimmest subsample L4 has a strong overabundance of galaxies around $z \sim 0.25$. We have validated that this overabundance is present at all angular positions. It might thus result from an interplay of the HOD-SHAM methodology used for assigning magnitudes and colors to galaxies and the LOWZ sample selection, leading to a preferred selection of objects at that redshift.

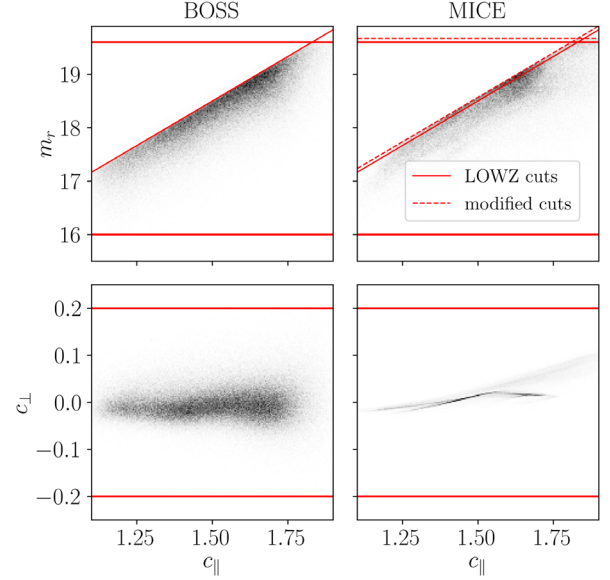


FIG. 20. LOWZ selection cuts in BOSS and MICE (left and right, respectively) on the apparent SDSS r -band magnitude m_r and the color cuts c_{\perp} and c_{\parallel} , as defined in Eq. (20). The m_r cut for MICE is slightly shifted to dimmer magnitudes in order to match the BOSS LOWZ number density, as indicated by the red dotted line in the top right panel.

Further investigations are needed to fully understand this effect. However, we do not expect this overabundance to significantly affect our measurements of the projected correlations w_{gg} and w_{g+} since it is isotropic and therefore taken into account in the random catalogs used in the estimators (see Sec. II).

2. DES-like samples

We verify the selection of the DES-like catalog in MICE by comparing the distributions of apparent magnitudes in the r , i , and z DES bands from the DES Y3 data and the remapped MICE photometry (described in Sec. III B) in Fig. 22. We find a reasonable agreement between MICE and DES Y3, with MICE containing a slightly longer tail toward bright objects. The DES Y3 distributions in that figure employ the fiducial quality cuts described in Gatti and Sheldon *et al.*, [44], plus an extra cut removing objects in Metacalibration with magnitude $i > 23$ to enable a closer comparison with the MICE photometry, which is limited at that magnitude.¹⁵

In Fig. 23, we display the $u - r$ color index (as defined in Sec. III C) versus the absolute SDSS r -band magnitude for the DES-like redshift samples from MICE, showing how a significant fraction of central galaxies are defined as blue according to the color cut used in our modeling

¹⁴<https://data.sdss.org/sas/dr11/boos/lss/>.

¹⁵Note that the $i < 23$ cut does not affect the comparison to COSMOS data in Fig. 1 since this is based on MICE galaxies in an area, which is complete down to $i < 24$.

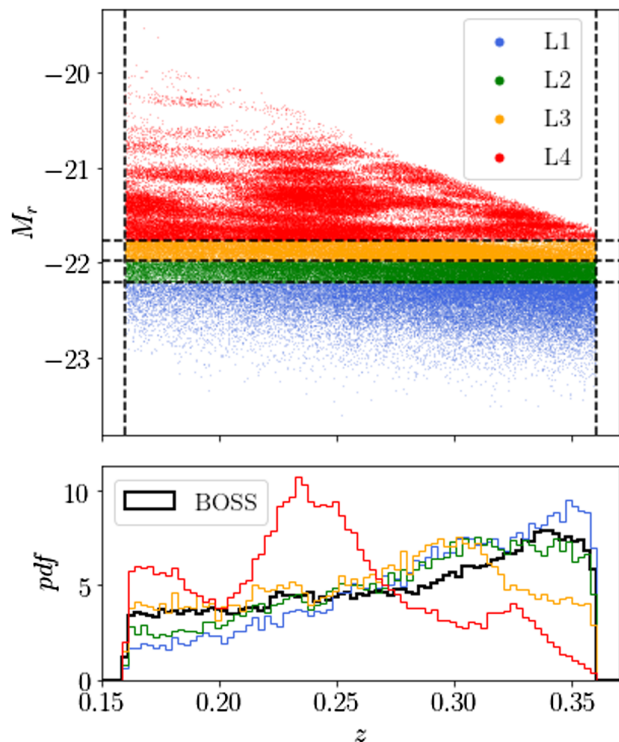


FIG. 21. Top: Absolute SDSS r -band magnitude versus redshift of galaxies in the mock BOSS LOWZ catalog. The LOWZ sample is split into four luminosity subsamples (L1-L4, from bright to faint) by quantiles, following SM16. The sample limits in redshift and magnitude are shown as dashed vertical and horizontal lines respectively. Bottom: Redshift distribution of the MICE luminosity samples in the same color coding as in the top panel. The black line shows the observed distribution of the entire LOWZ sample from BOSS DR11.

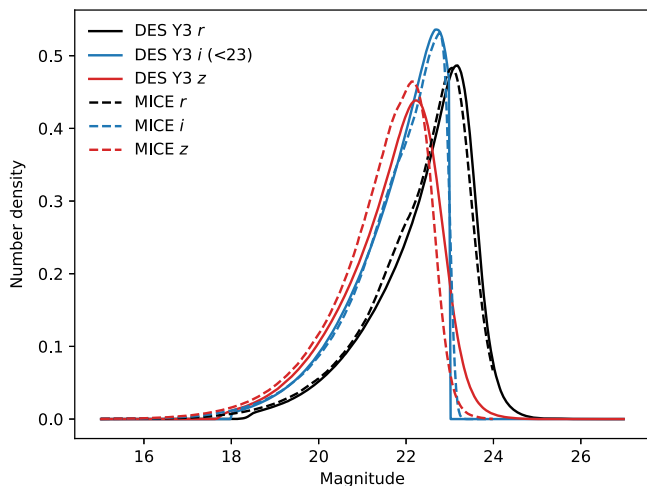


FIG. 22. Comparison between magnitude distributions on the DES Y3 Metacalibration catalog and the MICE photometry in riz bands. We introduce an extra apparent magnitude cut of $i < 23$ to METACALIBRATION in this comparison, matching MICE specifications.

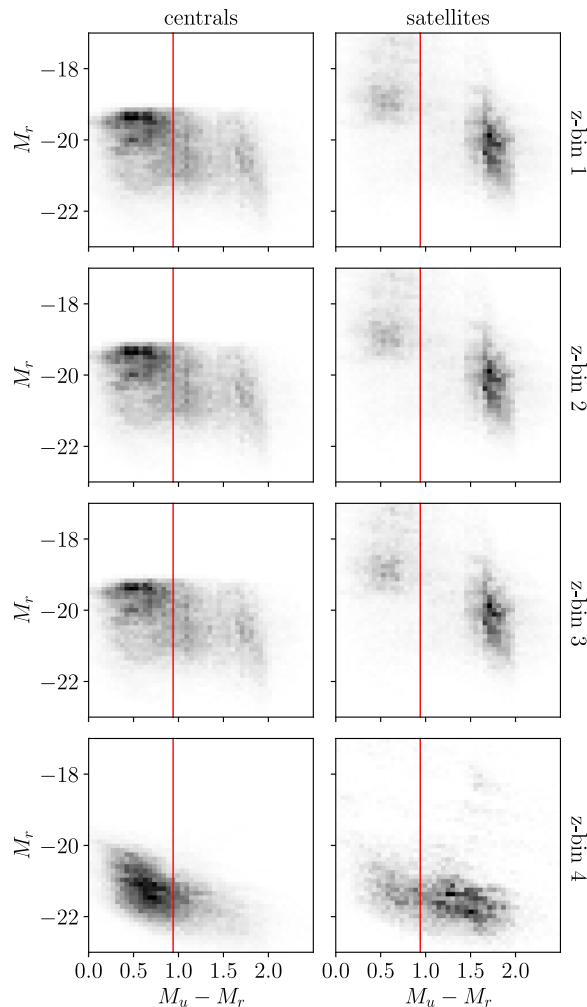


FIG. 23. Normalized distribution of the $u-r$ rest frame color index versus absolute r -band magnitude in four redshift bins of the DES-like samples with $i < 23$. Red lines indicate the color cut used to define red and blue galaxies in the IA modeling.

(see Table II). Figure 23 further reveals a lack of central galaxies dimmer than $M_r \sim -19$. This cutoff results from the fact that we require halos to have at least 10 particles. This condition imposes an absolute magnitude limit that affects only central galaxies as a consequence of the HOD-SHAM model with which galaxies are generated in MICE.¹⁶ Due to the apparent magnitude limit in the DES-like samples of $i < 23$, this artifact affects mainly centrals in the two lowest redshift bins 1 and 2 of the DES-like samples. The $i < 23$ cut on the other hand affects a significant fraction of centrals as well as satellites in the two highest redshift bins 3 and 4.

Both the $M_r \sim -19$ and the $i = 23$ cuts can potentially boost the IA amplitude, as they remove centrals in low mass

¹⁶Note here that this lack of galaxies in low mass halos only affects the MICE IA catalog, not the full simulated catalog, for which FoF halos down to two particles were populated with galaxies.

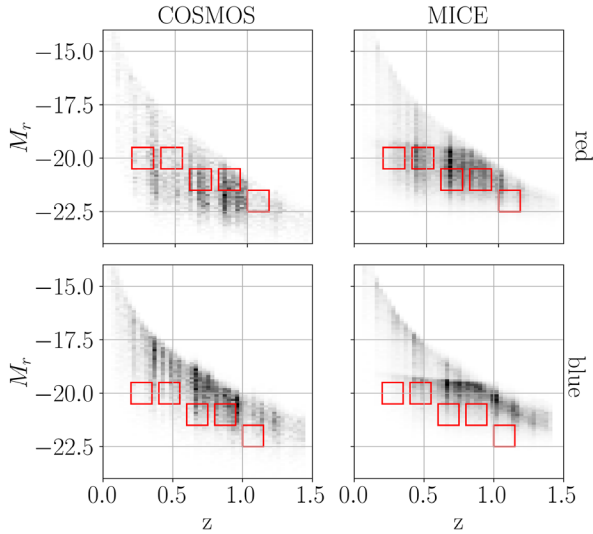


FIG. 24. Normalized distribution of absolute Subaru r -band magnitudes in COSMOS and MICE for red and blue galaxies. The set of volume limited subsamples used for comparing the axis ratio distributions in Fig. 6 are marked by red rectangles. The drop in the density for galaxies in MICE with $M_r > -20$ results from a lack of host halos with less than 10 particles (see discussion Sec. III E).

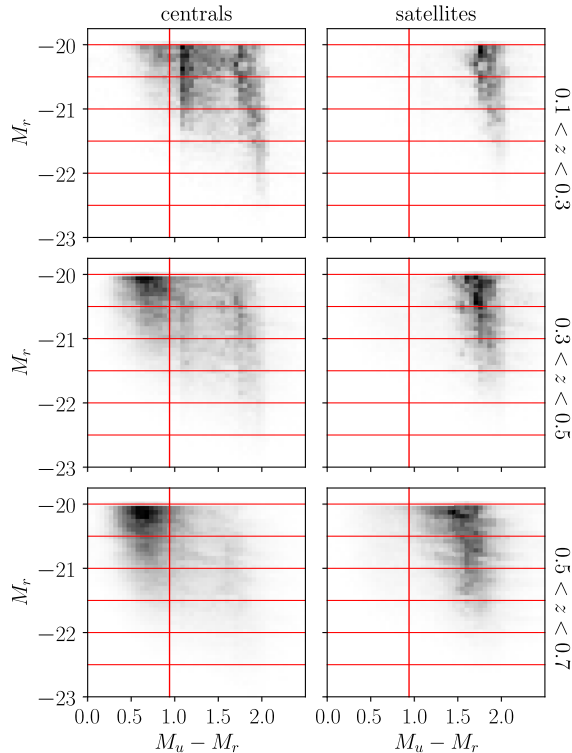


FIG. 25. Normalized distribution of the $u - r$ rest frame color index versus absolute r -band magnitude in three redshift bins of the MICE simulation. Red dashed lines indicate the limits of the color-redshift samples used for the measuring predictions for w_{m+} (Fig. 12).

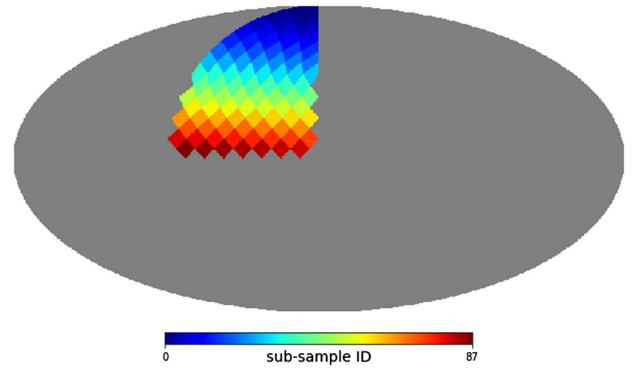


FIG. 26. Healpix regions ($N_{\text{side}} = 8$) in the MICE octant, used for the jackknife estimation of the covariance for w_{g+} and w_{m+} .

halos as well as faint satellites. Centrals in low mass halos should be weakly aligned due to a decrease in halo alignment with decreasing mass [91], and, moreover, the noise in measured orientations increases as the number of halo particles decreases. Satellites with faint absolute magnitudes have more randomized orientations than bright satellites, according to our semianalytic IA model (Sec. V). Removing such highly randomized objects from the sample could hence increase the amplitude of the IA statistics. However, investigating the magnitude of such an increase would require a higher resolution simulation that is complete below to $i = 23$. In this work, we therefore regard the IA signal predicted by MICE for the DES-like samples as an upper bound for an IA signal that we would measure when including galaxies in halos with less than 10 particles and apparent magnitudes below $i = 23$.

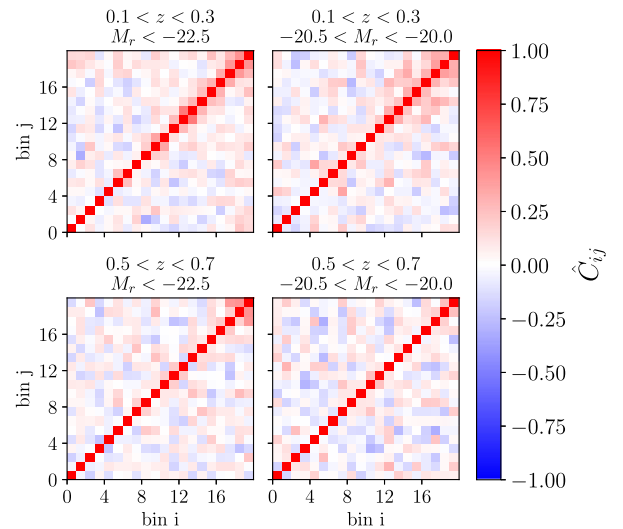


FIG. 27. Jack-knife estimates of the normalized covariance matrix $\hat{C}_{ij} \equiv C_{ij}/(\sigma_i\sigma_j)$ for w_{m+} measurements in the bins i and j . Results are shown for red galaxies in four of our volume limited samples.

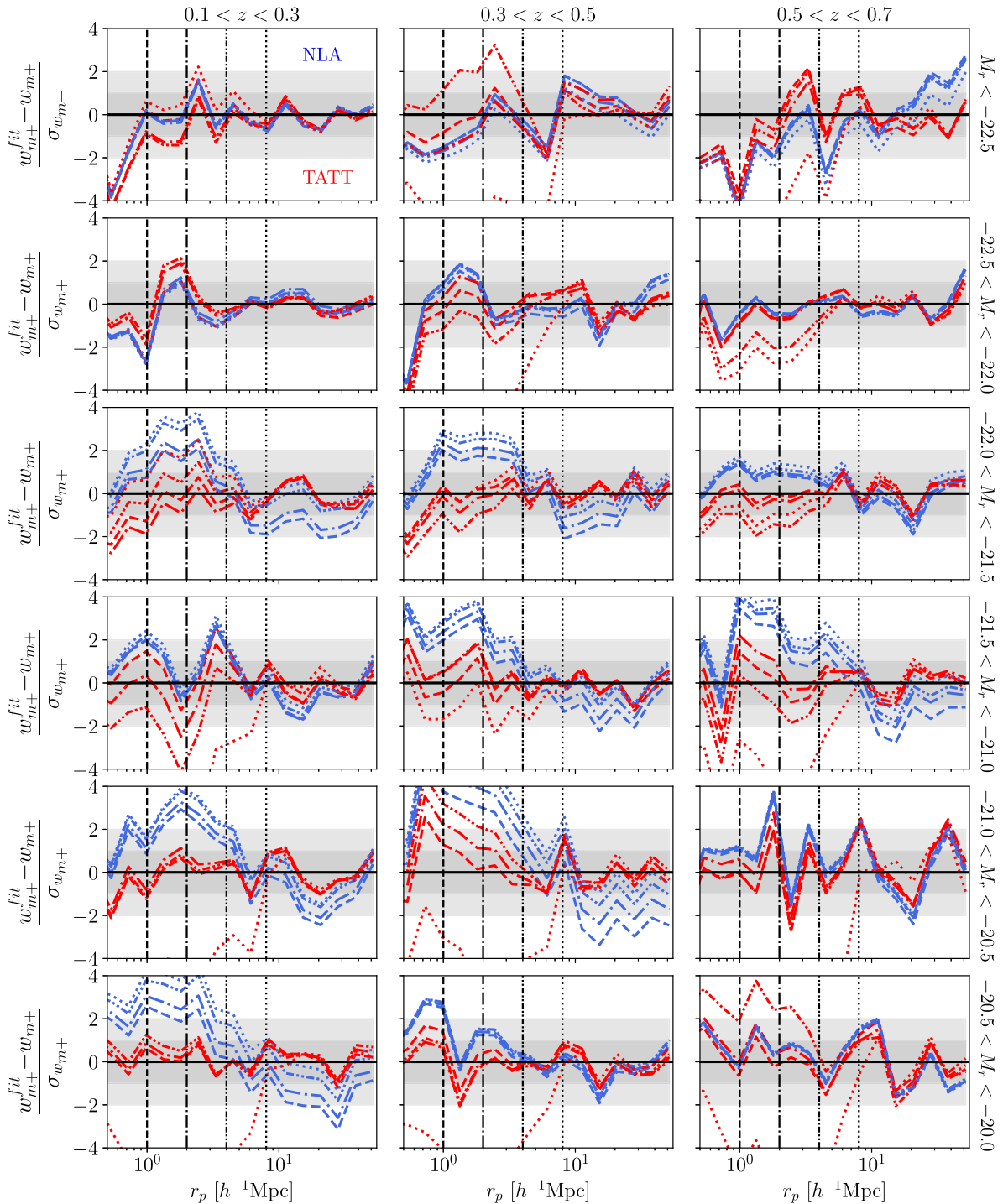


FIG. 28. Significance of the deviations between the w_{m+} measurements, shown in Fig. 12, and fits to the NLA and the TATT model. Results are shown for 16 volume limited samples whose redshift and magnitude ranges are indicated on the top and right, respectively. Dashed, dashed-dotted, dashed-double dotted, and dotted lines are results derived for different lower limits of the fitting range, which are set to $r_p^{\min} = 1, 2, 4, 8 h^{-1}$ Mpc, respectively. These limits are indicated by the vertical lines in the corresponding line types. The upper limit of the fitting range is set to $r_p^{\max} = 60 h^{-1}$ Mpc.

3. Volume limited sample selection

The selection of volume limited samples, used to compare the galaxy axis ratio distributions in COSMOS

and MICE (Sec. IV), is illustrated in Fig. 24, separately for red and blue galaxies. Figure 25 shows the selection of the volume limited samples that are used to study the redshift,

magnitude, and color dependence of the IA statistics in MICE (Sec. VI A), separately for central and satellite galaxies.

APPENDIX C: JACKKNIFE COVARIANCE

Our delete-one jackknife estimates of the covariance matrix of the projected correlations, described in Sec. II A 1, are derived from angular subsamples, which are defined as healpix pixels with $N_{\text{side}} = 8$. The area covered by the different subsamples in the MICE octant is shown in Fig. 26. In Fig. 27, we show examples of the normalized covariance estimated for w_{m+} measurements in four of our 16 volume limited samples. We find that all covariances are dominated by the diagonal elements, while the off-diagonal elements are noisy, which potentially affects the fits of the NLA and the TATT model predictions for w_{m+} to the measurements.

APPENDIX D: SCALE DEPENDENCE OF TATT PARAMETERS

We investigate here how well the NLA and the TATT model predictions for w_{m+} fit the measurements over different ranges of the transverse distance scale r_p . In addition, we study how variations in the fitting range affect the inferred model parameters. For that purpose, we perform

the Bayesian parameter inference, described in Sec. VI B, for the lower limits of $r_p^{\text{min}} \in [1, 2, 4, 8]h^{-1}\text{Mpc}$ and the upper limits of $r_p^{\text{max}} \in [30, 60]h^{-1}\text{Mpc}$.

In Fig. 28, we show the significance of the deviations between $w_{m+}(r_p)$ measurements and fits, defined as the absolute difference over the standard deviation, for different r_p^{min} and a fixed value of $r_p^{\text{max}} = 60h^{-1}\text{Mpc}$. Results are shown for the same 16 volume limited sample of red galaxies as in Fig. 12. Note that we do not investigate results for blue samples since their alignment signal is consistent with zero by construction. The results in Fig. 28 show that the fits of the TATT model do not deviate by more than 2σ from the measurements within the scale range over which the fit is performed. This is true even for $r_p^{\text{min}} = 1h^{-1}\text{Mpc}$, which we therefore choose as lower scale cut for the fits shown in Fig. 12. In addition, we find that the fitting performance of the TATT model at large scales ($r_p > 8h^{-1}\text{Mpc}$) is only weakly affected by the small scale cut. The results for the TATT model are contrasted by those for the NLA model. For this model, we find strong deviations of more than 4σ when fitting between 1 and $60h^{-1}\text{Mpc}$. The fitting performance at large scales is thereby strongly affected by the lower scale cut, indicating a lack of flexibility in the model. However, when restricting the lower scale cut to $r_p^{\text{min}} = 8h^{-1}\text{Mpc}$, we find the NLA model to fit the measurements with a similar 2σ

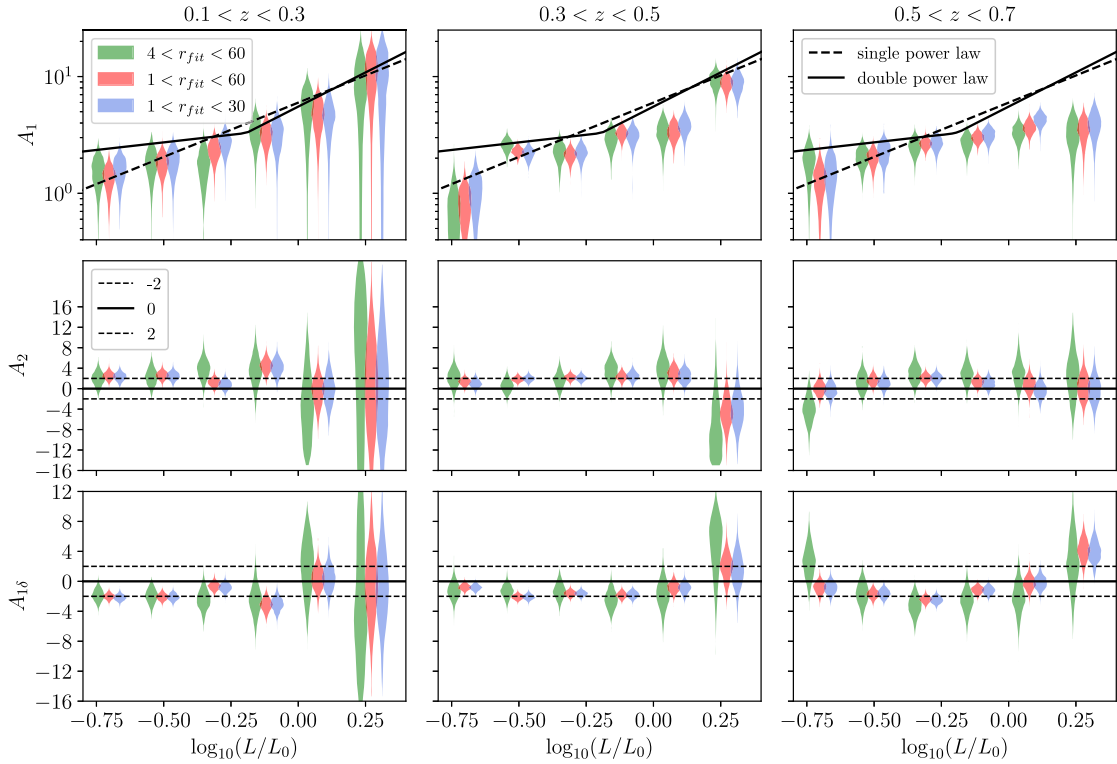


FIG. 29. Marginalized posterior distributions of the TATT model parameters from fits to w_{m+} measurements in different volume limited samples of red galaxies in MICE versus each sample's logarithmic normalized mean r -band luminosity (analogous to Fig. 15). Results are shown for different scale ranges used for the fits, as indicated in the top left panel in units of $h^{-1}\text{Mpc}$.

uncertainty as the TATT model. This scale cut is therefore chosen for the NLA fits shown in Fig. 12. It is further interesting to note that there is no clear dependence of the fitting performance on either magnitude or redshift and hence on the amplitude of w_{m+} .

In Fig. 29, we show the parameters of the TATT model versus the luminosity of the different volume limited

samples in three redshift bins. We find no significant change of the parameters when changing the upper (lower) limit of the fiducial fitting range of $1 < r_p^{\max} = 60 h^{-1}$ Mpc to $4 (30) h^{-1}$ Mpc. This finding shows that the conclusions drawn from Fig. 15 are robust toward moderate variations of the chosen fitting range.

-
- [1] T. M. C. Abbott *et al.*, *Phys. Rev. D* **105**, 023520 (2022).
- [2] C. Heymans *et al.*, *Astron. Astrophys.* **646**, A140 (2021).
- [3] C. Hikage *et al.*, *Publ. Astron. Soc. Jpn.* **71**, 43 (2019).
- [4] B. Joachimi *et al.*, *Space Sci. Rev.* **193**, 1 (2015).
- [5] A. Kiessling *et al.*, *Space Sci. Rev.* **193**, 67 (2015).
- [6] D. Kirk *et al.*, *Space Sci. Rev.* **193**, 139 (2015).
- [7] M. A. Troxel and M. Ishak, *Phys. Rep.* **558**, 1 (2015).
- [8] E. Krause, T. Eifler, and J. Blazek, *Mon. Not. R. Astron. Soc.* **456**, 207 (2016).
- [9] J. A. Blazek, N. MacCrann, M. A. Troxel, and X. Fang, *Phys. Rev. D* **100**, 103506 (2019).
- [10] P. Catelan, M. Kamionkowski, and R. D. Blandford, *Mon. Not. R. Astron. Soc.* **320**, L7 (2001).
- [11] R. G. Crittenden, P. Natarajan, U.-L. Pen, and T. Theuns, *Astrophys. J.* **559**, 552 (2001).
- [12] M. C. Fortuna, H. Hoekstra, B. Joachimi, H. Johnston, N. Elisa Chisari, C. Georgiou, and C. Mahony, *Mon. Not. R. Astron. Soc.* **501**, 2983 (2021).
- [13] C. M. Hirata and U. Seljak, *Phys. Rev. D* **70**, 063526 (2004).
- [14] M. C. Fortuna *et al.*, *Astron. Astrophys.* **654**, A76 (2021).
- [15] C. M. Hirata, R. Mandelbaum, M. Ishak, U. Seljak, R. Nichol, K. A. Pimbblet, N. P. Ross, and D. Wake, *Mon. Not. R. Astron. Soc.* **381**, 1197 (2007).
- [16] B. Joachimi, R. Mandelbaum, F. B. Abdalla, and S. L. Bridle, *Astron. Astrophys.* **527**, A26 (2011).
- [17] H. Johnston *et al.*, *Astron. Astrophys.* **624**, A30 (2019).
- [18] H. Johnston *et al.*, *Astron. Astrophys.* **646**, A147 (2021).
- [19] R. Mandelbaum, C. M. Hirata, M. Ishak, U. Seljak, and J. Brinkmann, *Mon. Not. R. Astron. Soc.* **367**, 611 (2006).
- [20] R. Mandelbaum *et al.*, *Mon. Not. R. Astron. Soc.* **410**, 844 (2011).
- [21] S. Singh and R. Mandelbaum, *Mon. Not. R. Astron. Soc.* **457**, 2301 (2016).
- [22] S. Singh, R. Mandelbaum, and S. More, *Mon. Not. R. Astron. Soc.* **450**, 2195 (2015).
- [23] S. Codis, A. Jindal, N. E. Chisari, D. Vibert, Y. Dubois, C. Pichon, and J. Devriendt, *Mon. Not. R. Astron. Soc.* **481**, 4753 (2018).
- [24] N. Chisari, N. Chisari, S. Codis, C. Laigle, Y. Dubois, C. Pichon, J. Devriendt, A. Slyz, L. Miller, R. Gavazzi, and K. Benabed, *Mon. Not. R. Astron. Soc.* **454**, 2736 (2015).
- [25] S. Hilbert, D. Xu, P. Schneider, V. Springel, M. Vogelsberger, and L. Hernquist, *Mon. Not. R. Astron. Soc.* **468**, 790 (2017).
- [26] S. Samuroff, R. Mandelbaum, and J. Blazek, *Mon. Not. R. Astron. Soc.* **508**, 637 (2021).
- [27] A. Tenneti, R. Mandelbaum, T. Di Matteo, A. Kiessling, and N. Khandai, *Mon. Not. R. Astron. Soc.* **453**, 469 (2015).
- [28] M. Velliscig *et al.*, *Mon. Not. R. Astron. Soc.* **454**, 3328 (2015).
- [29] R. A. C. Croft and C. A. Metzler, *Astrophys. J.* **545**, 561 (2000).
- [30] A. Heavens, A. Refregier, and C. Heymans, *Mon. Not. R. Astron. Soc.* **319**, 649 (2000).
- [31] C. Heymans, M. Brown, A. Heavens, K. Meisenheimer, A. Taylor, and C. Wolf, *Mon. Not. R. Astron. Soc.* **347**, 895 (2004).
- [32] F. C. van den Bosch, T. Abel, R. A. C. Croft, L. Hernquist, and S. D. M. White, *Astrophys. J.* **576**, 21 (2002).
- [33] C. Heymans, M. White, A. Heavens, C. Vale, and L. Van Waerbeke, *Mon. Not. R. Astron. Soc.* **371**, 750 (2006).
- [34] T. Okumura and Y. P. Jing, *Astrophys. J.* **694**, L83 (2009).
- [35] T. Okumura, Y. P. Jing, and C. Li, *Astrophys. J.* **694**, 214 (2009).
- [36] B. Joachimi, E. Semboloni, P. E. Bett, J. Hartlap, S. Hilbert, H. Hoekstra, P. Schneider, and T. Schrabback, *Mon. Not. R. Astron. Soc.* **431**, 477 (2013).
- [37] B. Joachimi, E. Semboloni, S. Hilbert, P. E. Bett, J. Hartlap, H. Hoekstra, and P. Schneider, *Mon. Not. R. Astron. Soc.* **436**, 819 (2013).
- [38] A. Knebe, N. Draganova, C. Power, G. Yepes, Y. Hoffman, S. Gottlöber, and B. K. Gibson, *Mon. Not. R. Astron. Soc.* **386**, L52 (2008).
- [39] C. Wei *et al.*, *Astrophys. J.* **853**, 25 (2018).
- [40] M. Crocce, F. J. Castander, E. Gaztañaga, P. Fosalba, and J. Carretero, *Mon. Not. R. Astron. Soc.* **453**, 1513 (2015).
- [41] P. Fosalba, E. Gaztañaga, F. J. Castander, and M. Crocce, *Mon. Not. R. Astron. Soc.* **447**, 1319 (2015).
- [42] P. Fosalba, M. Crocce, E. Gaztañaga, and F. J. Castander, *Mon. Not. R. Astron. Soc.* **448**, 2987 (2015).
- [43] S. Bridle and L. King, *New J. Phys.* **9**, 444 (2007).
- [44] M. Gatti *et al.*, *Mon. Not. R. Astron. Soc.* **504**, 4312 (2021).
- [45] B. Joachimi and P. Schneider, *Astron. Astrophys.* **517**, A4 (2010).
- [46] S. D. Landy and A. S. Szalay, *Astrophys. J.* **412**, 64 (1993).
- [47] M. Jarvis, G. Bernstein, and B. Jain, *Mon. Not. R. Astron. Soc.* **352**, 338 (2004).

- [48] L. F. Secco *et al.*, *Phys. Rev. D* **105**, 023515 (2022).
- [49] X. Fang, J. A. Blazek, J. E. McEwen, and C. M. Hirata, *J. Cosmol. Astropart. Phys.* **02** (2017) 030.
- [50] J. E. McEwen, X. Fang, C. M. Hirata, and J. A. Blazek, *J. Cosmol. Astropart. Phys.* **09** (2016) 015.
- [51] E. Krause *et al.*, arXiv:2105.13548.
- [52] C. Laigle *et al.*, *Astron. Astrophys. Suppl. Ser.* **224**, 24 (2016).
- [53] R. L. Griffith *et al.*, *Astrophys. J. Suppl. Ser.* **200**, 9 (2012).
- [54] K. Hoffmann, C. Laigle, N. E. Chisari, P. Tallada-Crespí, R. Teyssier, Y. Dubois, and J. Devriendt, *Mon. Not. R. Astron. Soc.* **515**, 3603 (2022).
- [55] O. Ilbert *et al.*, *Astron. Astrophys.* **457**, 841 (2006).
- [56] O. Ilbert *et al.*, *Astrophys. J.* **690**, 1236 (2009).
- [57] B. Häußler *et al.*, in *Astronomical Data Analysis Software and Systems XX*, edited by I. N. Evans *et al.*, Astronomical Society of the Pacific Conference Series Vol. 442 (Astronomical Society of the Pacific, 2011), p. 155.
- [58] V. Springel, *Mon. Not. R. Astron. Soc.* **364**, 1105 (2005).
- [59] P. Fosalba, E. Gaztañaga, F. J. Castander, and M. Manera, *Mon. Not. R. Astron. Soc.* **391**, 435 (2008).
- [60] J. Carretero, F. J. Castander, E. Gaztañaga, M. Crocce, and P. Fosalba, *Mon. Not. R. Astron. Soc.* **447**, 646 (2015).
- [61] M. R. Blanton *et al.*, *Astrophys. J.* **592**, 819 (2003).
- [62] I. Zehavi *et al.*, *Astrophys. J.* **736**, 59 (2011).
- [63] F. Pitié, A. C. Kokaram, and R. Dahyot, in *Proceedings of the Tenth IEEE International Conference on Computer Vision (ICCV'05) Volume 1, Beijing, China* (IEEE, New York, 2005), p. 1434.
- [64] J. De Vicente, E. Sánchez, and I. Sevilla-Noarbe, *Mon. Not. R. Astron. Soc.* **459**, 3078 (2016).
- [65] I. Sevilla-Noarbe *et al.*, *Astron. Astrophys. Suppl. Ser.* **254**, 24 (2021).
- [66] V. Springel, S. D. M. White, G. Tormen, and G. Kauffmann, *Mon. Not. R. Astron. Soc.* **328**, 726 (2001).
- [67] E. J. Gonzalez *et al.*, arXiv:2205.06827.
- [68] R. Guo, C.-N. Hao, X. Xia, Y. Shi, Y. Chen, S. Li, and Q. Gu, *Astrophys. J.* **897**, 162 (2020).
- [69] A. W. Graham and C. C. Worley, *Mon. Not. R. Astron. Soc.* **388**, 1708 (2008).
- [70] K. S. Dawson *et al.*, *Astron. J.* **145**, 10 (2013).
- [71] M. A. Troxel *et al.*, *Phys. Rev. D* **98**, 043528 (2018).
- [72] J. Myles *et al.*, *Mon. Not. R. Astron. Soc.* **505**, 4249 (2021).
- [73] J. Binney, *Mon. Not. R. Astron. Soc.* **183**, 501 (1978).
- [74] D. G. Lambas, S. J. Maddox, and J. Loveday, *Mon. Not. R. Astron. Soc.* **258**, 404 (1992).
- [75] P. D. Noerdlinger, *Astrophys. J.* **234**, 802 (1979).
- [76] B. S. Ryden, *Astrophys. J.* **601**, 214 (2004).
- [77] A. Sandage, K. C. Freeman, and N. R. Stokes, *Astrophys. J.* **160**, 831 (1970).
- [78] G. M. Bernstein and M. Jarvis, *Astron. J.* **123**, 583 (2002).
- [79] F. Bertola, M. Vietri, and W. W. Zeilinger, *Astrophys. J. Lett.* **374**, L13 (1991).
- [80] J. E. Huizinga and T. S. van Albada, *Mon. Not. R. Astron. Soc.* **254**, 677 (1992).
- [81] H.-W. Rix and D. Zaritsky, *Astrophys. J.* **447**, 82 (1995).
- [82] D. Freedman and P. Diaconis, *Z. Wahrscheinlichkeitstheorie Verw. Gebiete* **57**, 453 (1981).
- [83] D. Foreman-Mackey, D. W. Hogg, D. Lang, and J. Goodman, *Publ. Astron. Soc. Pac.* **125**, 306 (2013).
- [84] S. Rodríguez and N. D. Padilla, *Mon. Not. R. Astron. Soc.* **434**, 2153 (2013).
- [85] P. Bett, *Mon. Not. R. Astron. Soc.* **420**, 3303 (2012).
- [86] A. K. Bhowmick, Y. Chen, A. Tenneti, T. Di Matteo, and R. Mandelbaum, *Mon. Not. R. Astron. Soc.* **491**, 4116 (2020).
- [87] N. E. Chisari *et al.*, *Mon. Not. R. Astron. Soc.* **472**, 1163 (2017).
- [88] S. Samuroff *et al.*, *Mon. Not. R. Astron. Soc.* **489**, 5453 (2019).
- [89] C. Hirata and U. Seljak, *Mon. Not. R. Astron. Soc.* **343**, 459 (2003).
- [90] R. Reyes, R. Mandelbaum, J. E. Gunn, R. Nakajima, U. Seljak, and C. M. Hirata, *Mon. Not. R. Astron. Soc.* **425**, 2610 (2012).
- [91] D. Piras, B. Joachimi, B. Malte Schäfer, M. Bonamigo, S. Hilbert, and E. van Uitert, *Mon. Not. R. Astron. Soc.* **474**, 1165 (2018).
- [92] J. Blazek, Z. Vlah, and U. Seljak, *J. Cosmol. Astropart. Phys.* **08** (2015) 015.
- [93] J. Hartlap, P. Simon, and P. Schneider, *Astron. Astrophys.* **464**, 399 (2007).
- [94] J. Bate *et al.*, *Mon. Not. R. Astron. Soc.* **491**, 4057 (2020).
- [95] A. Amon *et al.*, *Phys. Rev. D* **105**, 023514 (2022).
- [96] X. Fang, T. Eifler, and E. Krause, *Mon. Not. R. Astron. Soc.* **497**, 2699 (2020).
- [97] W. J. Handley, M. P. Hobson, and A. N. Lasenby, *Mon. Not. R. Astron. Soc.* **453**, 4384 (2015).
- [98] C. Georgiou *et al.*, *Astron. Astrophys.* **622**, A90 (2019).
- [99] H.-J. Huang, R. Mandelbaum, P. E. Freeman, Y.-C. Chen, E. Rozo, and E. Rykoff, *Mon. Not. R. Astron. Soc.* **474**, 4772 (2018).
- [100] A. Knebe, M. Gámez-Marín, F. R. Pearce, W. Cui, K. Hoffmann, M. De Petris, C. Power, R. Hagggar, and R. Mostoghiu, *Mon. Not. R. Astron. Soc.* **495**, 3002 (2020).
- [101] S. Pyne and B. Joachimi, *Mon. Not. R. Astron. Soc.* **503**, 2300 (2021).
- [102] D. M. Schmitz, C. M. Hirata, J. Blazek, and E. Krause, *J. Cosmol. Astropart. Phys.* **07** (2018) 030.
- [103] L. F. Secco *et al.*, *Phys. Rev. D* **105**, 103537 (2022).
- [104] J. Carretero *et al.*, *Proc. Sci. EPS-HEP2017* (2017) 488.
- [105] P. Tallada *et al.*, *Astron. Comput.* **32**, 100391 (2020).
- [106] J. E. Forero-Romero, S. Contreras, and N. Padilla, *Mon. Not. R. Astron. Soc.* **443**, 1090 (2014).
- [107] M. A. Aragon-Calvo and L. F. Yang, *Mon. Not. R. Astron. Soc.* **440**, L46 (2014).
- [108] J. Lee and N. I. Libeskind, *Astrophys. J.* **902**, 22 (2020).
- [109] B. Reid *et al.*, *Mon. Not. R. Astron. Soc.* **455**, 1553 (2016).